

Diversifying NMR Supersequences with New HSQC-based Modules

Jonathan R. J. Yong,¹ Alexandar L. Hansen,² Ēriks Kupče,³ Tim D. W. Claridge^{1,*}

¹ *Chemistry Research Laboratory, Department of Chemistry, University of Oxford, Mansfield Road, Oxford, OX1 3TA, U.K.*

² *Campus Chemical Instrument Center, The Ohio State University, 460 W. 12th Avenue, Columbus, OH, 43210 U.S.*

³ *Bruker UK Ltd., Banner Lane, Coventry, CV4 9GH, U.K.*

* tim.claridge@chem.ox.ac.uk

Abstract

The sensitivity-enhanced HSQC, as well as HSQC-TOCSY, experiments have been modified for incorporation into NOAH (NMR by Ordered Acquisition using ¹H detection) supersequences, adding diversity for ¹³C and ¹⁵N modules. Importantly, these heteronuclear modules have been specifically tailored to preserve the magnetisation required for subsequent acquisition of other heteronuclear or homonuclear modules in a supersequence. In addition, we present protocols for optimally combining HSQC and HSQC-TOCSY elements within the same supersequences, yielding high-quality 2D spectra suitable for structure characterisation but with greatly reduced experiment durations. We further demonstrate that these time-savings can translate to increased detection sensitivity per unit time.

In recent years, there has been significant interest in the acceleration of multidimensional NMR data acquisition.^[1–5,6e] In particular, some of the more readily implemented methods involve multiple-FID experiments which use either single or multiple receivers. Of these, one of the most versatile approaches is to utilise different “pools” of magnetisation available within a sample for the sequential collection of different spectra without an intervening recovery delay, as exemplified by the NOAH (NMR by Ordered Acquisition using ¹H detection) technique.^[6] Virtually all of the most

common 2D experiments used in small molecule characterisation, such as HSQC, HMBC, COSY, TOCSY, NOESY, and ROESY, can be combined in a modular fashion to form *supersequences* which collectively use only one recovery delay (d_1) (Figure 1a). As the recovery delay accounts for the large majority of experiment time in 2D NMR, the NOAH approach can provide time savings of up to $\sim 4\times$ compared to the conventional individual acquisition of each spectrum, where each constituent experiment would require its own recovery delay.

One-bond heteronuclear correlation experiments, namely HSQC and HMQC, play a central role in the structural elucidation of small organic molecules and biomolecules.^[7] These experiments are also a core component of many NOAH experiments, since the magnetisation they use (protons directly coupled to isotopically dilute X nuclei, i.e. ^{13}C or ^{15}N) can be efficiently differentiated from the “bulk” magnetisation of protons that are not directly attached to these NMR-active nuclei.^[8] Following the notation of Orts,^[9] we refer to these two magnetisation components (proton coupled to X and proton not coupled to X) as $^1\text{H}^X$ and $^1\text{H}^{!X}$ respectively. At the same time, due to the low natural abundance of these heteronuclei, these spectra are typically less sensitive than the homonuclear spectra that are placed towards the end of the supersequence. Consequently, for dilute samples, the minimum experimental time is generally dictated by these heteronuclear experiments, meaning any improvements in experiment sensitivity can be directly translated into greater time savings.

In the 1990s, Cavanagh, Rance, and Kay introduced the sensitivity-enhanced HSQC (seHSQC) experiment,^[10] which improves on the sensitivity of an ordinary echo–antiecho HSQC by up to a factor of 2 in the most ideal case. This is accomplished through the so-called preservation of equivalent pathways (PEP) scheme, which converts two magnetisation components that are cosine- and sine-modulated in t_1 into observable magnetisation prior to detection.^[11] Here, we show how the original seHSQC sequence can be modified such that it can be used as a NOAH module. We add further diversification by incorporating a HSQC-TOCSY module, derived from the ASAP-HSQC-TOCSY,^[1j] that is also compatible with the NOAH strategy. Both of these modules can be inserted either independently or together into NOAH supersequences, allowing large amounts of chemical information to be acquired in short times.

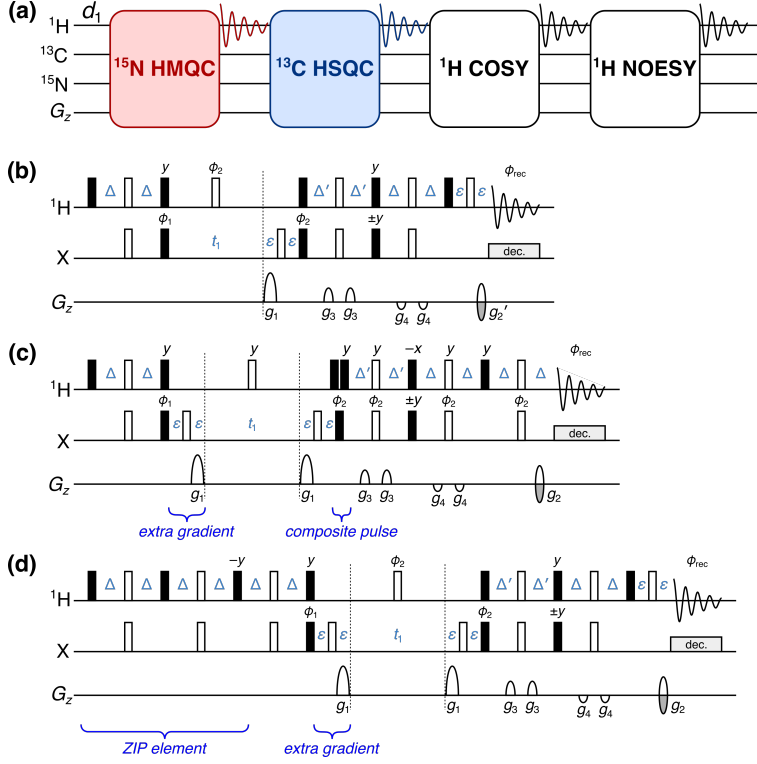


Figure 1: (a) Overview of a typical NOAH supersequence (MSCN, using the single-letter abbreviations previously defined^[6a]). The ¹⁵N–¹H HMQC and ¹³C–¹H HSQC modules are coloured; these may be replaced with the new seHSQC module proposed in this work. (b) Cavanagh–Rance–Kay (CRK) seHSQC.^[10] (c) Version 1 of the NOAH seHSQC module, abbreviated as “S₁⁺”. (d) Version 2 of the NOAH seHSQC module (“ZIP-seHSQC”), abbreviated as “S₂⁺”. Filled and unfilled bars represent 90° and 180° pulses respectively; all 180° pulses on ¹³C are adiabatic (frequency-swept) pulses. All pulses are applied along +x unless otherwise noted. Phase cycling is performed with $\phi_1 = (x, -x)$, $\phi_2 = (x, x, -x, -x)$, and $\phi_{rec} = (x, -x, -x, x)$. The delays are chosen as follows: $\Delta = 1/(4 \cdot {}^1J_{\text{XH}})$, $\Delta' = 1/(8 \cdot {}^1J_{\text{CH}})$ or $1/(4 \cdot {}^1J_{\text{NH}})$, and ε is the minimum time needed for a gradient pulse and subsequent recovery. All gradient pulses are 1 ms long, except for g_1 and g_2 in ¹⁵N experiments which are 2.5 ms long. Gradient amplitudes, as percentages of maximum gradient strength, are as follows: $g_1 = 80\%$; $g_2 = \pm 40.2\%$ (¹³C) or $\pm 16.2\%$ (¹⁵N); $g_2' = g_2/2$; $g_3 = 11\%$; $g_4 = -5\%$. The signs of g_2 and g_2' , as well as the phase of the 90° X pulse marked $\pm y$, are alternated within each t_1 increment to provide echo–antiecho selection. Refer to Figure S1 for product operator analysis.

A typical example of a NOAH supersequence is the NOAH-4 MSCN experiment (Figure 1a), which yields ¹⁵N HMQC, ¹³C HSQC, COSY, and NOESY spectra in one single experiment.^[6a] The implementation of this supersequence relies on the fact that the output of any one module contains all the necessary magnetisation components required for downstream modules. For example, both the standard NOAH HMQC (Figure S1a)^[1c,6a] and HSQC (Figure S1b)^[1h,6a] modules return the bulk ¹H^{IX} magnetisation back to its equilibrium position (+z). In the MSCN sequence, this bulk magnetisation can therefore be used as the input to the COSY and NOESY homonuclear modules

which follow. However, the original Cavanagh–Rance–Kay (CRK) seHSQC (Figure 1b) does not obey this principle: it causes bulk magnetisation to be dephased by coherence transfer pathway (CTP) gradients. Consequently, downstream modules can only utilise any bulk $^1\text{H}^{!X}$ magnetisation that has relaxed during the HSQC FID acquisition, leading to drastic losses in signal intensity. This is illustrated using a NOAH-2 S⁺C^c (seHSQC + CLIP-COSY^[12]) supersequence (Figure 2a): the CLIP-COSY is used in this work as a convenient module for which peaks can be easily integrated, but the conclusions drawn here are fully applicable to any other homonuclear module that is used in its place. While the CRK seHSQC implementation (Figure 2b) affords significant sensitivity gains (primarily for CH peaks, as predicted by theory^[13]), the COSY module which follows suffers from an almost complete ($\sim 90\%$) loss of intensity. While one could argue that this is still tolerable for the COSY module, which is the most sensitive of all NOAH modules, these losses are not permissible for less inherently sensitive homonuclear modules such as NOESY and ROESY.

In this work, we compare two possible solutions to this, which form the basis of the NOAH seHSQC modules. In both cases, we require a pulse sequence element which performs a selective 90° rotation on $^1\text{H}^X$ magnetisation and leaves $^1\text{H}^{!X}$ magnetisation untouched. The first version of the NOAH seHSQC (Figure 1c, “S₁⁺”) uses a composite ^1H pulse immediately following t_1 to accomplish this aim, as both magnetisation components have already diverged by this point. On the other hand, the second (Figure 1d, “S₁⁺” or “ZIP-seHSQC”) actively differentiates the two components at the start of the sequence by prepending a double heteronuclear spin echo, a strategy recently reported by Hansen *et al.*^[15] This zz isotope-selective (ZIP) pulse element is based on the observation that the bulk $^1\text{H}^{!X}$ magnetisation in the seHSQC will be returned to $+z$ if the phase of the initial ^1H 90_x° pulse in the CRK seHSQC is changed by 90° to $+y$. To generate the required HSQC signal, however, a ^1H 90_x° pulse must still be applied to $^1\text{H}^X$ magnetisation. Overall, what is required is therefore a pulse sequence element which simultaneously acts as a 90_x° (or 90_{-x}°) pulse on protons coupled to spin-X, and as a 90_y° pulse on uncoupled protons. The resulting ZIP element is similar to the zz -filter, which has previously been used in the NOAH zz -HMBC module to retain the magnetisation of directly coupled protons for a subsequent HSQC module.^[6b,6d] However, the ZIP element has different pulse phases to this and consequently leads to a different overall outcome, i.e.

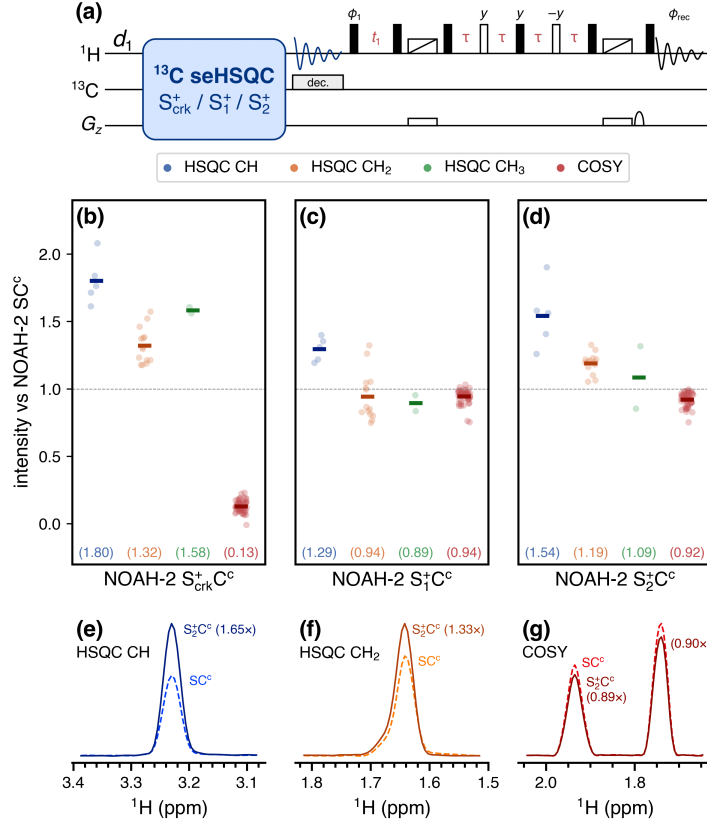


Figure 2: Sensitivity comparisons for NOAH-2 $S^+ C^c$ (seHSQC + CLIP-COSY) supersequences, using the CRK and NOAH seHSQC implementations. The delay Δ' was set to $1/(8 \cdot {}^1J_{CH})$. All intensities are normalised against the NOAH-2 SC^c (HSQC + CLIP-COSY) supersequence, without HSQC sensitivity enhancement. HSQC intensities are further grouped by multiplicity. Circles represent the relative intensities of individual peaks; solid bars, as well as the numbers in parentheses, indicate averages over all peaks of a given type. (a) Pulse sequence of the NOAH-2 $S^+ C^c$ (seHSQC + CLIP-COSY) experiment: any of the variants shown in Figure 1 (CRK, version 1, or version 2/“ZIP”) can be used as the seHSQC module. The CLIP-COSY^[12] is performed with $\phi_1 = \phi_{rec} = (x, -x)$ and States quadrature detection in the indirect dimension; the perfect echo mixing delay τ is set to 8.33 ms. The unfilled rectangles with diagonal lines, applied simultaneously with z -gradients, represent frequency-swept pulses used for suppression of zero-quantum coherence.^[14] (b) Using the original CRK seHSQC (Figure 1b), which leads to severely reduced COSY intensities. (c) Using the S_1^+ module (Figure 1c). (d) Using the S_2^+ module (Figure 1d). (e)–(f) Slices of the NOAH HSQC (dashed line) and NOAH ZIP-seHSQC (S_2^+) spectra (solid line) through $f_1 = 78.9$ ppm (a CH peak, (e)) and $f_1 = 28.5$ ppm (a CH₂ peak, (f)). (g) Slices of the CLIP-COSY module from the NOAH-2 SC^c (dashed line) and $S_2^+ C^c$ (solid line) supersequences, through $f_1 = 1.36$ ppm. Spectra were obtained on a 700 MHz Bruker AV III equipped with a TCI H/C/N cryoprobe; the sample used was 40 mM andrographolide in DMSO-*d*₆.

90°_x on ${}^1H^X$ and 90°_y on ${}^1H^{IX}$.

In addition to the aforementioned modifications, both NOAH seHSQC modules also contain a CTP

gradient prior to the t_1 period (highlighted in Figures 1c and 1d). In the S_1^+ module, the ${}^1\text{H}^{1\text{X}}$ magnetisation is in the xy -plane during t_1 (see Figure S1 for product operator analysis), and would simply be dephased if this gradient were not present, making its presence mandatory. Alternatively, the S_2^+ module places the ${}^1\text{H}^{1\text{X}}$ magnetisation on $\pm z$ in t_1 . This gradient is therefore not used for rephasing, but instead serves to suppress artefacts in downstream modules, which would otherwise arise from bulk magnetisation that (due to pulse imperfections) is *not* longitudinal and can therefore evolve during either half of the HSQC t_1 period (Figures S2 to S4). This magnetisation then evolves again in the t_1 period of a later homonuclear module (e.g. COSY), resulting in each COSY peak with indirect-dimension frequency $f_1 = \Omega_{\text{H}}$ being accompanied by a pair of “wing” artefacts at $f_1 = \Omega_{\text{H}} \pm (\Omega_{\text{H}} \cdot \text{SW}_{\text{COSY}})/(2 \cdot \text{SW}_{\text{HSQC}})$, where Ω_{H} and SW refer to the proton offset and indirect-dimension spectral width respectively (both in Hz). Importantly, the artefacts arising from diagonal peaks can have intensities that are comparable to genuine crosspeaks (Figure S2), which highlights the importance of suppressing these artefacts. Apart from the “wing” artefacts in downstream modules, we also briefly note here that the presence of two CTP gradients inside the seHSQC t_1 period allows the final CTP gradient (g_2) to have twice its usual amplitude, thereby providing additional artefact suppression in the seHSQC itself. This is particularly important in the ${}^{15}\text{N}-{}^1\text{H}$ seHSQC, as will be explained below.

These pulse sequence modifications result in an unavoidable decrease in efficiency, as compared to the original CRK seHSQC implementation (Figures 2b to 2d). For example, with the present sample, when the delay Δ' is set to $1/(8 \cdot {}^1J_{\text{CH}})$ as was done here,^[13a] the S_1^+ and S_2^+ modules yield on average a $1.29\times$ and $1.54\times$ boost for CH peaks, which are smaller than the $1.80\times$ increase seen with the CRK seHSQC (the case where $\Delta' = 1/(4 \cdot {}^1J_{\text{CH}})$ is explored in Figures S5 and S6). Turning to CH_2 and CH_3 peaks, the use of the S_1^+ module does not provide any enhancement for either of these, whilst the S_2^+ module yields on average a more modest $1.19\times$ and $1.09\times$ sensitivity increase respectively. Nevertheless, it should be emphasised that the S_2^+ module in particular still provides clear sensitivity gains over the reference “gold-standard” NOAH HSQC module, especially for CH and CH_2 peaks (Figures 2e and 2f).

The major advantage that the NOAH seHSQC modules enjoy over the CRK seHSQC is readily

appreciated when considering the homonuclear module which follows. In contrast to the CRK seHSQC, which destroys the requisite bulk $^1\text{H}^{!X}$ magnetisation and is thus unsuitable for use in NOAH supersequences, both of the new seHSQC modules preserve the majority of it, performing >90% as well as the original HSQC module (Figure 2g). Altogether, this means that the HSQC intensities in a NOAH supersequence can be substantially boosted using the new seHSQC modules, without compromising the sensitivity of, or introducing extra artefacts in, any homonuclear modules which succeed it. We note that the BIG-BIRD element reported by Briand and Sørensen,^[8d] which independently excites $^1\text{H}^X$ and $^1\text{H}^{!X}$ magnetisation with arbitrary flip angles and phases, is also capable of performing the same role as the ZIP element in the S_2^+ module. However, we find that the ZIP provides greater signal-to-noise in both the seHSQC itself as well as downstream modules (Figure S7).

Multiplicity editing^[16] can be easily incorporated into both NOAH seHSQC modules (Figure S8) by introducing a J -evolution period in the spin echo immediately following t_1 . As described previously, the S_1^+ module places the bulk magnetisation in the xy -plane during the editing period; the same is true of the unenhanced NOAH HSQC. In these modules, the bulk $^1\text{H}^{!X}$ magnetisation is therefore subject to homonuclear coupling (J_{HH}) evolution, leading to a small decrease in the sensitivity of later homonuclear modules when multiplicity editing is introduced. Since homonuclear experiments typically have a greater inherent sensitivity than the (se)HSQC, this minor loss is rarely a problem, and is far outweighed by the benefits of incorporating multiplicity editing in the HSQC. Nevertheless, the fact that the S_2^+ module does not suffer from such a penalty is a welcome benefit. As a result, when editing is included, the S_2^+ module slightly outperforms both the S and S_1^+ modules by around 10% in terms of preserving bulk magnetisation (Figure S9).

The proposed seHSQC modules can be similarly implemented as $^1\text{H}-^{15}\text{N}$ experiments. Currently, in NOAH supersequences, $^1\text{H}-^{15}\text{N}$ correlations are primarily obtained using the HMQC module (“M”);^[1c,6a] compared to this, the new S_2^+ module can provide greater than 4× enhanced sensitivity (Figure 3). This arises partly because the PEP sensitivity enhancement scheme can be optimised for NH peaks by setting the reverse INEPT transfer delay Δ' to be equal to $1/(4 \cdot ^1J_{\text{NH}})$. However, there is also a significant improvement due to the fact that peaks in the ^{15}N seHSQC are not split

in the indirect dimension by J_{HH} , unlike in the HMQC. Although the S_2^+ module retains a slightly smaller amount of ${}^1\text{H}^{15}\text{N}$ magnetisation ($\sim 70\%$, versus $\sim 80\%$ for the HMQC (Figure S10)), this is a worthwhile trade-off, since it is the ${}^{15}\text{N}$ module which typically has the lowest intrinsic sensitivity in a supersequence.

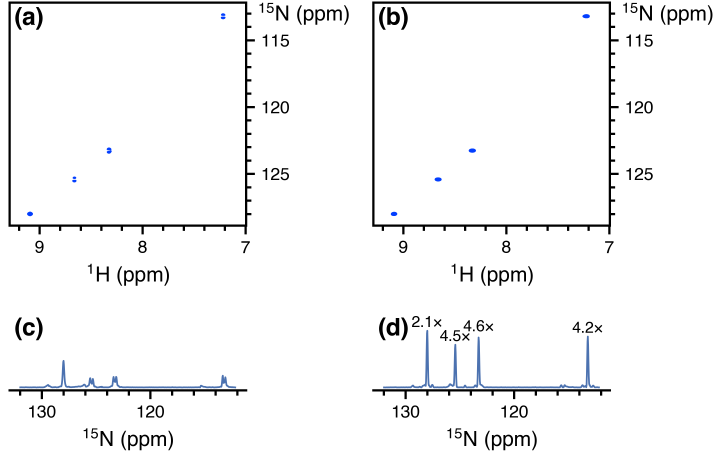


Figure 3: Comparison of the ${}^{15}\text{N}-{}^1\text{H}$ seHSQC module (S_2^+) with the standard NOAH HMQC module (M), taken from NOAH-3 XS^+C^c supersequences (${}^{15}\text{N}$ experiment + ${}^{13}\text{C}$ seHSQC + CLIP-COSY). The S_1^+ module is not shown here as it causes line broadening in downstream modules (see text). (a) ${}^{15}\text{N}$ HMQC spectrum. (b) ${}^{15}\text{N}$ seHSQC spectrum. (c) Projection of HMQC onto the f_1 axis. Splitting due to J_{HH} is clearly visible for three of the four peaks. (d) Projection of seHSQC onto the f_1 axis. Sensitivity improvements relative to the HMQC spectrum (as measured by peak heights) are indicated above each peak. The largest gains are observed for peaks where the multiplet structure is collapsed; however, even in the absence of that, a $\sim 2\times$ gain is still obtained. Spectra were obtained on a 700 MHz Bruker AV III equipped with a TCI H/C/N cryoprobe; the sample used was 40 mM gramicidin (a cyclic decapeptide; (Val–Orn–Leu–D-Phe–Pro)₂) in DMSO- d_6 .

Although the S and S_1^+ modules also provide sensitivity gains versus the HMQC, they both come with other drawbacks. As previously discussed, these two modules place bulk ${}^1\text{H}^{15}\text{N}$ magnetisation in the xy -plane during the t_1 period. Consequently, the amount of bulk magnetisation that is retained decreases as t_1 is lengthened, leading to line broadening in the indirect dimensions of all downstream modules (Figure S11). Whilst this is not a problem with the ${}^{13}\text{C}$ HSQC where typical ${}^{13}\text{C}$ indirect dimension acquisition times are relatively short, the smaller spectral widths in ${}^{15}\text{N}$ experiments can mean downstream modules suffer moderate losses in both sensitivity and resolution. The S_2^+ module avoids this issue entirely, making it especially well-suited to obtaining ${}^{15}\text{N}$ correlations; we henceforth refer to it as the S_N^+ module.

One remaining potential issue in the S_N^+ module arises from the cumulative effects of pulse imperfections, which cause a portion of bulk $^{1H}^{15N}$ magnetisation to be transverse just prior to detection of the seHSQC signal. Although this only represents a small fraction of the bulk magnetisation, if left uncontrolled, the resulting artefacts typically have intensities that are comparable to the seHSQC crosspeaks (Figure S12). The key to suppressing these artefacts efficiently lies in the final CTP gradient g_2 (Figure 1d), which dephases any transverse bulk magnetisation. The S_N^+ module therefore greatly benefits from having two CTP gradients g_1 within the t_1 period, as this means that g_2 will have twice its usual amplitude. For optimal performance, however, one further modification proves beneficial: the CTP gradients g_1 and g_2 should all be lengthened from their typical duration of 1 ms, in order to provide more effective dephasing. In practice, we find that gradient durations of 2 to 2.5 ms provide excellent artefact suppression whilst not causing any appreciable difference in the intensity of the desired crosspeaks (Figure S12). These extended gradients are not required in the ^{13}C seHSQC for two reasons: firstly, the amplitude of g_2 in the ^{13}C seHSQC is larger by a factor of $\gamma_C/\gamma_N \approx 2.5$; and secondly, the greater natural abundance of ^{13}C (1.1% versus 0.36% of ^{15}N) leads to an intrinsically larger signal intensity, which makes any residual artefacts less apparent.

In scenarios where high resolution in the ^{15}N dimension is not required, it is possible to reduce the indirect-dimension (F_1) resolution in order to obtain sensitivity gains. This can be done either by increasing the F_1 spectral width by a factor of k (“SW-scaling”), or by reducing the number of t_1 increments by a factor of k and in its place increasing the number of transients (“ k -scaling”):^[3d,3e] both of these cause equivalent reductions of the F_1 acquisition time and thus resolution (Figure S13). When implemented within a supersequence, this scaling is applied exclusively to the ^{15}N module: all other modules are left untouched. In our hands, significant sensitivity gains of up to $\sim 2\times$ can be observed in SW- and k -scaled ^{15}N HMQC spectra, since J_{HH} splitting in the indirect dimension tends not to be resolved (Figure S14). This point is not relevant to the seHSQC, and here, any scaling employed in isolation has only a small effect on peak height, since any peak volume gained from the extra transients is typically offset by the broadening (Figure S15). It is possible to use linear prediction^[17] to counteract this broadening, thereby improving the signal-to-noise ratio

(SNR) of the resulting spectra (Figures S16 and S17). We note, however, that SNR improvements obtained purely via processing methods such as linear prediction should not be conflated with an increase in the true detection sensitivity of the spectrum.^[18]

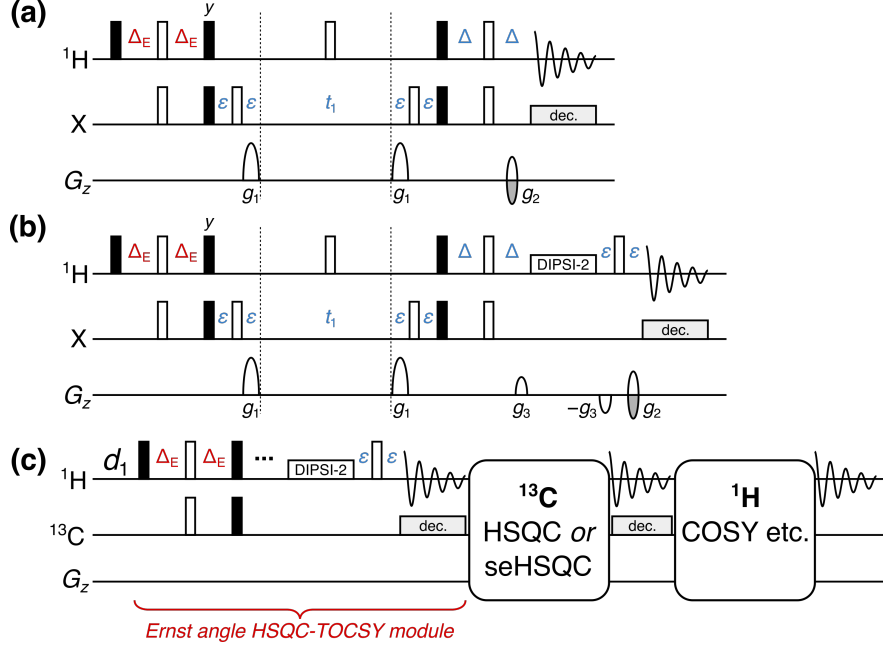


Figure 4: (a) NOAH HSQC module with modified INEPT delay $\Delta_E = (\sin^{-1} f)/(4 \cdot {}^1J_{\text{CH}})$, where f is the fraction of ${}^1\text{H}^{\text{C}}$ magnetisation excited. (b) NOAH HSQC-TOCSY module ("S^T"), modified from the ASAP-HSQC-TOCSY.^[1j] The gradients g_3 are 1 ms long, and are set to 19% of the maximum gradient amplitude. (c) Overview of a NOAH-3 S^TSX or S^TS⁺X supersequence. The ${}^1\text{H}^{\text{C}}$ magnetisation is partly used by the initial HSQC-TOCSY module, with a subsequent HSQC or seHSQC using the remaining ${}^1\text{H}^{\text{C}}$ magnetisation. The bulk ${}^1\text{H}^{\text{C}}$ magnetisation is retained for one or more homonuclear modules at the end. All other symbols have the same meanings as in Figure 1.

Thus far, we have described seHSQC modules which utilise all of the ${}^1\text{H}^{\text{X}}$ magnetisation. However, it is often desirable to draw on ${}^1\text{H}^{\text{C}}$ magnetisation for multiple different purposes: for example, one can simultaneously collect ${}^{13}\text{C}$ -decoupled and coupled HSQC spectra,^[19a] HSQC spectra with different spectral widths,^[19b] or a combination of HSQC and HSQC-TOCSY spectra.^[19a] This has previously been accomplished in a multi-FID acquisition (MFA) scheme by keeping the two CTPs in the CRK seHSQC separate, with the cosine- and sine-modulated CTPs each contributing to one spectrum.^[19] We chose to adopt a different approach for NOAH supersequences, which exploits the fact that the HSQC module (though not the new seHSQC modules) allows an arbitrary amount of ${}^1\text{H}^{\text{C}}$ magnetisation to be excited, with the remainder returned to $+z$.^[1c,1g,1h,1i] In order

to excite a proportion f of $^1\text{H}^{\text{C}}$ magnetisation ($0 < f \leq 1$), the initial INEPT delay must be shortened by a factor of $\sin^{-1} f$ (Figure 4a). The remaining $(1 - f)$ of the magnetisation, plus any that relaxes during the HSQC FID, can then be used for a *second* HSQC-based module in the same supersequence. With the present NOAH strategy, for values of f close to 1, the amount of $^1\text{H}^{\text{C}}$ magnetisation regained through relaxation can reach almost 50%. Consequently, by setting $f \approx 0.8$, we can obtain two HSQC spectra with sensitivities that are comparable to the existing MFA approach. Furthermore, the sensitivity of the second HSQC can be boosted by using the new seHSQC modules in its place, in particular the S_2^+ module (Figure S18).

By adding a period of isotropic mixing prior to detection, the NOAH HSQC module may be converted to a HSQC-TOCSY module (denoted by “ S^T ”, Figure 4b). This is similar to the previously reported ASAP-HSQC-TOCSY,^[1j] the key difference being that in the present NOAH context, unused $^1\text{H}^{\text{C}}$ as well as bulk $^1\text{H}^{\text{C}}$ magnetisation is preserved for use in other modules, instead of later t_1 increments as in the ASAP experiment. Compared to the existing MFA HSQC-TOCSY/HSQC experiment,^[19a] our approach has several characteristics which make it particularly amenable to use in NOAH supersequences. Firstly, the vast majority of $^1\text{H}^{\text{C}}$ magnetisation is preserved, as required for homonuclear module(s) to be appended in a NOAH supersequence (Figure 4c); in practice, we observe small $^1\text{H}^{\text{C}}$ losses of ca. 10% due to pulse imperfections. In contrast, the MFA sequence, much like the original CRK seHSQC on which it is based, dephases $^1\text{H}^{\text{C}}$ magnetisation and causes a 80–90% sensitivity loss in downstream spectra. Secondly, since each NOAH module is independently executed, the NOAH approach allows multiplicity editing to be selectively enabled for only the HSQC and not the HSQC-TOCSY, where accidental overlap may lead to crosspeaks being lost unexpectedly. Lastly, the sensitivity of both spectra in a NOAH experiment can be optimised through the value of f ; this allows a larger amount of $^1\text{H}^{\text{C}}$ magnetisation to be used for the inherently less sensitive HSQC-TOCSY. In our experience, setting $f = 0.9$ provides a good balance for S^T s combinations: the sensitivity in the HSQC is boosted not only by relaxation during the HSQC-TOCSY FID, but also by the isotropic mixing in the HSQC-TOCSY module, which effects a degree of $^1\text{H}^{\text{C}} \rightarrow ^1\text{H}^{\text{C}}$ polarisation transfer (Figure S19). Alternatively, the signal intensity of the HSQC-TOCSY can be maximised by replacing it with the seHSQC-TOCSY module, derived

from the S_2^+ module.^[15] The seHSQC-TOCSY does still retain $^{1\text{H}}\text{C}$ magnetisation needed for the terminal homonuclear module(s), but has a minor drawback in that it does not allow for variable $^{1\text{H}}\text{C}$ excitation and therefore cannot preserve a portion of $^{1\text{H}}\text{C}$ magnetisation for HSQC modules that follow it (Figure S20).

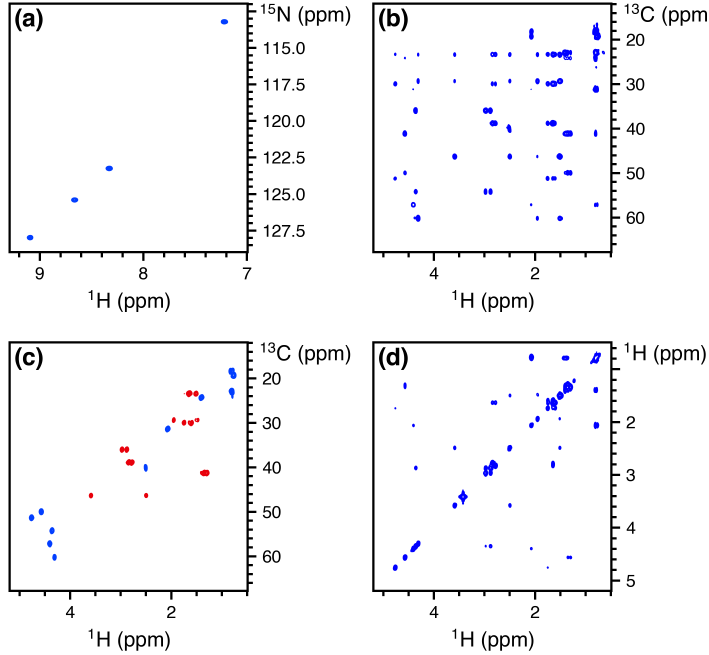


Figure 5: Spectra obtained from the NOAH-4 $S_N^+S^T S_2^+ C^c$ supersequence. 256 t_1 increments were used, with 2 scans per increment. The total experiment time was 17 minutes and 35 seconds. (a) ^{15}N seHSQC. (b) ^{13}C HSQC-TOCSY (30 ms mixing, $f = 0.9$). (c) Multiplicity-edited ^{13}C ZIP-seHSQC. Notice that having the edited seHSQC removes the need for the less desirable HSQC-TOCSY editing. (d) CLIP-COSY. Spectra were obtained on a 700 MHz Bruker AV III equipped with a TCI H/C/N cryoprobe; the sample used was 40 mM gramicidin in $\text{DMSO}-d_6$.

There exist many ways in which the new modules discussed above can be included in practical experiments for structure characterisation. Here, we illustrate this with the NOAH-4 $S_N^+S^T S_2^+ C^c$ (^{15}N seHSQC, ^{13}C HSQC-TOCSY, ^{13}C seHSQC, and CLIP-COSY) supersequence (Figure 5). While individual collection of the four spectra above required 57 minutes and 8 seconds, the NOAH-4 supersequence took only 17 minutes and 35 seconds; this is 31% of the original duration, or equivalently a 3.3 \times speedup. For typical organic molecules, new supersequences such as the NOAH-4 $S^T S_2^+ CT$ allow the rapid and complete collection of C–H and H–H correlations (Figure S21). Experiment times can be further reduced through the use of non-uniform sampling^[20] (Figure S22),

which is compatible with nearly all of the supersequences shown here (the exceptions being when k -scaling is employed in ^{15}N modules, or when COSY modules are recorded without phase-sensitive detection). One can also prepend the NOAH zz -HMBC module (“B”);^[6b,6d] this uses the semi-adiabatic zz -filter to preserve both $^1\text{H}^{\text{C}}$ and $^1\text{H}^{\text{N}}$ magnetisation, which can then be sampled in the HSQC-based modules presented here (Figure S23).

The benefits of the time savings afforded by NOAH supersequences are manifold. On top of the greatly increased sample throughput that results from faster acquisition, the combination of multiple modules in a single experiment also ensures that all constituent spectra are recorded under the same experimental conditions, such as temperature. This avoids the need for separate chemical shift referencing in each spectrum, and also makes the real-time monitoring and characterisation of reactive intermediates possible, especially when combined with non-uniform sampling. It is also of note that time savings may be directly translated into increases in sensitivity per unit time. The *relative sensitivity per unit time*, ε_t , of a given module is the product of an *amplitude factor* R_S indicating the intrinsic sensitivity of a module with respect to a reference experiment, and the square root of a *time-saving factor* ρ_t , which reflects the decrease in time needed for collection of all spectra.^[6d]

We demonstrate this with the NOAH-4 $\text{S}_\text{N}^+ \text{S}_2^+$ CT supersequence (experimental time of 17 minutes and 28 seconds), choosing individually acquired versions of the four constituent modules as the reference spectra (total experimental time of 58 minutes and 42 seconds), which gives $\rho_t = 3.36$. The amplitude factor R_S starts off at 1 for the first module, with a slight decrease as the supersequence progresses due to imperfections in magnetisation preservation. Nevertheless, ε_t remains well above 1 for all four modules (Figure 6), which clearly illustrates the attainable gains in sensitivity per unit time in NOAH sequences where R_S is not significantly compromised: this is especially important for the heteronuclear modules which are naturally less sensitive. Comparisons against “standard” experiments (such as the CRK seHSQC) lead to similar conclusions (Figure S24).

The new seHSQC and HSQC-TOCSY implementations add to the preexisting variety of NOAH modules, expanding the number of plausible NOAH supersequences tailored for small molecule

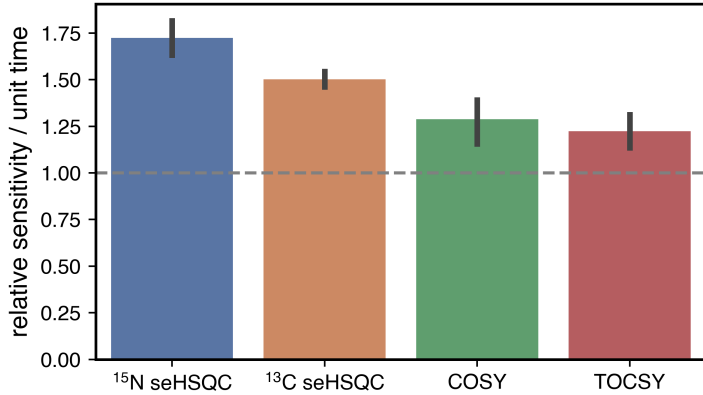


Figure 6: Relative sensitivities per unit time (ε_t) for the four modules in the $\text{S}_\text{N}^+\text{S}_\text{2}^+$ CT supersequence (using a TOCSY mixing time of 35 ms). Error bars indicate 95% confidence intervals. The four NOAH modules, individually acquired, were used as the reference spectra ($\rho_t = 3.36$). Spectra were obtained on a 700 MHz Bruker AV III equipped with a TCI H/C/N cryoprobe; the sample used was 50 mM zolmitriptan in $\text{DMSO}-d_6$.

characterisation. The controlled manipulation of all proton magnetisation reservoirs present within a sample is required for the success of these modules within nested experiments. We have demonstrated the optimisation of the individual HSQC-based modules and their combinations to further enhance the diversity of NOAH supersequences for efficient data collection.

Experimental

All spectra were recorded on a Bruker AV III NMR spectrometer operating at 700 MHz ^1H frequency equipped with a TCI H/C/N cryoprobe. Unless otherwise specified, spectra were recorded with 16 dummy scans, 2 scans per t_1 increment, 256 t_1 increments per module, and a 1.5 s recovery delay. 1024 points were recorded in each FID, leading to an acquisition time of 60.8–73.1 ms depending on the ^1H spectral width (10–12 ppm). Unless otherwise stated, indirect-dimension spectral widths were 180 ppm for ^{13}C modules, and 30 or 80 ppm for ^{15}N modules acquired on gramicidin and zolmitriptan respectively. The delays in the HSQC sequences were optimised for $^1J_{\text{CH}} = 145$ Hz and $^1J_{\text{NH}} = 90$ Hz respectively, and the CLIP-COSY mixing delay (τ in the Figure 2a) was set to 8.33 ms, corresponding to a nominal J_{HH} value of 30 Hz. DIPSI-2 mixing in the HSQC-TOCSY and TOCSY modules was applied with a B_1 amplitude of 10 kHz.

All NOAH data were processed using the `splitx.au` AU programme, available in the standard

Bruker TopSpin software, which separates the individual modules into different datasets; these were then individually processed with `noah_EXPT` AU programmes, which define other processing parameters such as window functions. All datasets were linear predicted up to 512 complex points in f_1 , then zero-filled to 1024 and 2048 complex points in f_1 and f_2 respectively. NUS experiments, such as that in Figure S22, can be set up using a Python script. The pulse sequences used here, all AU processing scripts, as well as the NUS Python script are available from the authors upon request, and will also be made available via the online Bruker User Library.

Acknowledgements

We thank Drs Mohammadali Foroozandeh (University of Oxford) and Peter Howe (Syngenta UK) for helpful discussions. J.R.J.Y. thanks the Clarendon Fund (University of Oxford) and the EP-SRC Centre for Doctoral Training in Synthesis for Biology and Medicine (EP/L015838/1) for a studentship, generously supported by AstraZeneca, Diamond Light Source, Defence Science and Technology Laboratory, Evotec, GlaxoSmithKline, Janssen, Novartis, Pfizer, Syngenta, Takeda, UCB, and Vertex. Other acknowledgements...

References

- [1] (a) P. Schanda, Ě. Kupče, B. Brutscher, *J. Biomol. NMR* **2005**, *33*, 199–211; (b) P. Schanda, H. Van Melckebeke, B. Brutscher, *J. Am. Chem. Soc.* **2006**, *128*, 9042–9043; (c) Ě. Kupče, R. Freeman, *Magn. Reson. Chem.* **2007**, *45*, 2–4; (d) P. Schanda, *Prog. Nucl. Magn. Reson. Spectrosc.* **2009**, *55*, 238–265; (e) J. Furrer, *Chem. Commun.* **2010**, *46*, 3396–3398; (f) B. Vitorge, G. Bodenhausen, P. Pelupessy, *J. Magn. Reson.* **2010**, *207*, 149–152; (g) D. SchulzeSünninghausen, J. Becker, B. Luy, *J. Am. Chem. Soc.* **2014**, *136*, 1242–1245; (h) D. SchulzeSünninghausen, J. Becker, M. R. M. Koos, B. Luy, *J. Magn. Reson.* **2017**, *281*, 151–161; (i) M. R. M. Koos, B. Luy, *J. Magn. Reson.* **2019**, *300*, 61–75; (j) J. Becker, M. R. M. Koos, D. SchulzeSünninghausen, B. Luy, *J. Magn. Reson.* **2019**, *300*, 76–83.
- [2] (a) L. Frydman, T. Scherf, A. Lupulescu, *Proc. Natl. Acad. Sci. U. S. A.* **2002**, *99*, 15858–15862; (b) P. Pelupessy, *J. Am. Chem. Soc.* **2003**, *125*, 12345–12350; (c) L. Frydman, A.

Lupulescu, T. Scherf, *J. Am. Chem. Soc.* **2003**, *125*, 9204–9217; (d) P. Giraudeau, L. Frydman, *Annu. Rev. Anal. Chem.* **2014**, *7*, 129–161; (e) M. Gal, M. Mishkovsky, L. Frydman, *J. Am. Chem. Soc.* **2006**, *128*, 951–956; (f) P. Giraudeau, Y. Shrot, L. Frydman, *J. Am. Chem. Soc.* **2009**, *131*, 13902–13903; (g) A. Herrera, E. Fernández-Valle, R. Martínez-Álvarez, D. Molero, Z. D. Pardo, E. Sáez, M. Gal, *Angew. Chem. Int. Ed.* **2009**, *48*, 6274–6277; (h) Z. D. Pardo, G. L. Olsen, M. E. Fernández-Valle, L. Frydman, R. Martínez-Álvarez, A. Herrera, *J. Am. Chem. Soc.* **2012**, *134*, 2706–2715; (i) K. J. Donovan, E. Kupče, L. Frydman, *Angew. Chem. Int. Ed.* **2013**, *52*, 4152–4155; (j) J.-N. Dumez, *Prog. Nucl. Magn. Reson. Spectrosc.* **2018**, *109*, 101–134; (k) B. Gouilleux, L. Rouger, P. Giraudeau, *Annu. Rep. NMR Spectrosc.* **2018**, *75*, 75–144.

- [3] (a) M. Sattler, M. Maurer, J. Schleucher, C. Griesinger, *J. Biomol. NMR* **1995**, *5*, 97–102; (b) P. Nolis, M. Pérez, T. Parella, *Magn. Reson. Chem.* **2006**, *44*, 1031–1036; (c) P. Nolis, M. Pérez-Trujillo, T. Parella, *Angew. Chem. Int. Ed.* **2007**, *46*, 7495–7497; (d) M. Pérez-Trujillo, P. Nolis, W. Bermel, T. Parella, *Magn. Reson. Chem.* **2007**, *45*, 325–329; (e) T. Parella, P. Nolis, *Concepts Magn. Reson.* **2010**, *36A*, 1–23; (f) P. Nolis, K. Motiram-Corral, M. Pérez-Trujillo, T. Parella, *J. Magn. Reson.* **2019**, *298*, 23–30.
- [4] (a) Ē. Kupče, R. Freeman, B. K. John, *J. Am. Chem. Soc.* **2006**, *128*, 9606–9607; (b) Ē. Kupče, R. Freeman, *J. Am. Chem. Soc.* **2008**, *130*, 10788–10792; (c) Ē. Kupče, R. Freeman, *J. Magn. Reson.* **2010**, *206*, 147–153; (d) Ē. Kupče, R. Freeman, *Magn. Reson. Chem.* **2010**, *48*, 333–336; (e) S. M. Pudakalakatti, A. Dubey, G. Jaipuria, U. Shubhashree, S. K. Adiga, D. Moskau, H. S. Atreya, *J. Biomol. NMR* **2014**, *58*, 165–173; (f) S. M. Pudakalakatti, A. Dubey, H. S. Atreya, *J. Chem. Sci.* **2015**, *127*, 1091–1097; (g) H. Kovacs, Ē. Kupče, *Magn. Reson. Chem.* **2016**, *54*, 544–560.
- [5] (a) K. Motiram-Corral, M. Pérez-Trujillo, P. Nolis, T. Parella, *Chem. Commun.* **2018**, *54*, 13507–13510; (b) V. M. R. Kakita, K. Rachineni, M. Bopardikar, R. V. Hosur, *J. Magn. Reson.* **2018**, *297*, 108–112; (c) T. M. Nagy, T. Gyöngyösi, K. E. Kövér, O. W. Sørensen, *Chem. Commun.* **2019**, *55*, 12208–12211; (d) P. Nolis, K. Motiram-Corral, M. Pérez-Trujillo, T. Parella, *ChemPhysChem* **2019**, *20*, 356–360; (e) P. Nolis, K. Motiram-Corral, M. Pérez-

- Trujillo, T. Parella, *J. Magn. Reson.* **2019**, *298*, 23–30; (f) P. Nolis, T. Parella, *Magn. Reson. Chem.* **2019**, *57*, S85–S94; (g) V. M. R. Kakita, R. V. Hosur, *RSC Adv.* **2020**, *10*, 21174–21179; (h) T. M. Nagy, K. E. Kövér, O. W. Sørensen, *J. Magn. Reson.* **2020**, *316*, 106767.
- [6] (a) Ě. Kupče, T. D. W. Claridge, *Angew. Chem. Int. Ed.* **2017**, *56*, 11779–11783; (b) Ě. Kupče, T. D. W. Claridge, *Chem. Commun.* **2018**, *54*, 7139–7142; (c) T. D. W. Claridge, M. Mayzel, Ě. Kupče, *Magn. Reson. Chem.* **2019**, *57*, 946–952; (d) Ě. Kupče, T. D. W. Claridge, *J. Magn. Reson.* **2019**, *307*, 106568; (e) Ě. Kupče, K. R. Mote, A. Webb, P. K. Madhu, T. D. W. Claridge, *Prog. Nucl. Magn. Reson. Spectrosc.* **2021**, DOI 10.1016/j.pnmrs.2021.03.001.
- [7] (a) T. D. W. Claridge, *High-Resolution NMR Techniques in Organic Chemistry*, 3rd ed., Elsevier, Amsterdam, **2016**; (b) J. Cavanagh, *Protein NMR Spectroscopy: Principles and Practice*, 2nd ed., Academic Press, Burlington, Mass., **2007**.
- [8] (a) J. R. Garbow, D. P. Weitekamp, A. Pines, *Chem. Phys. Lett.* **1982**, *93*, 504–509; (b) S. Wimperis, R. Freeman, *J. Magn. Reson.* **1984**, *58*, 348–353; (c) D. Uhrin, T. Liptaj, K. E. Kover, *J. Magn. Reson. Ser. A* **1993**, *101*, 41–46; (d) J. Briand, O. W. Sørensen, *J. Magn. Reson.* **1997**, *125*, 202–206; (e) J. Briand, O. W. Sørensen, *J. Magn. Reson.* **1998**, *135*, 44–49.
- [9] J. Orts, A. D. Gossert, *Methods* **2018**, *138–139*, 3–25.
- [10] (a) A. G. Palmer, J. Cavanagh, P. E. Wright, M. Rance, *J. Magn. Reson.* **1991**, *93*, 151–170; (b) L. Kay, P. Keifer, T. Saarinen, *J. Am. Chem. Soc.* **1992**, *114*, 10663–10665.
- [11] (a) J. Cavanagh, M. Rance, *J. Magn. Reson.* **1990**, *88*, 72–85; (b) J. Cavanagh, M. Rance, *Annu. Rep. NMR Spectrosc.* **1993**, *27*, 1–58.
- [12] M. R. M. Koos, G. Kummerlöwe, L. Kaltschnee, C. M. Thiele, B. Luy, *Angew. Chem. Int. Ed.* **2016**, *55*, 7655–7659.
- [13] (a) J. Schleucher, M. Schwendinger, M. Sattler, P. Schmidt, O. Schedletzky, S. J. Glaser, O. W. Sørensen, C. Griesinger, *J. Biomol. NMR* **1994**, *4*, 301–306; (b) G. Kontaxis, J. Stonehouse, E. D. Laue, J. Keeler, *J. Magn. Reson.* **1994**, *111*, 70–76.
- [14] M. J. Thrippleton, J. Keeler, *Angew. Chem. Int. Ed.* **2003**, *42*, 3938–3941.

- [15] A. L. Hansen, Ě. Kupče, D.-W. Li, L. Bruschweiler-Li, C. Wang, R. Brüschweiler, “2D NMR-based Metabolomics with HSQC/TOCSY NOAH Supersequences”, submitted for publication, **2021**.
- [16] T. Parella, F. Sánchez-Ferrando, A. Virgili, *J. Magn. Reson.* **1997**, *126*, 274–277.
- [17] (a) D. Tufts, R. Kumaresan, *IEEE Trans. Acoust. Speech Signal Process.* **1982**, *30*, 671–675; (b) J. J. Led, H. Gesmar, *Chem. Rev.* **1991**, *91*, 1413–1426; (c) P. Koehl, *Prog. Nucl. Magn. Reson. Spectrosc.* **1999**, *34*, 257–299.
- [18] (a) D. L. Donoho, I. M. Johnstone, A. S. Stern, J. C. Hoch, *Proc. Natl. Acad. Sci. U. S. A.* **1990**, *87*, 5066–5068; (b) A. S. Stern, K.-B. Li, J. C. Hoch, *J. Am. Chem. Soc.* **2002**, *124*, 1982–1993; (c) M. R. Palmer, C. L. Suiter, G. E. Henry, J. Rovnyak, J. C. Hoch, T. Polenova, D. Rovnyak, *J. Phys. Chem. B* **2015**, *119*, 6502–6515.
- [19] (a) P. Nolis, K. Motiram-Corral, M. Pérez-Trujillo, T. Parella, *ChemPhysChem* **2019**, *20*, 356–360; (b) P. Nolis, K. Motiram-Corral, M. Pérez-Trujillo, T. Parella, *J. Magn. Reson.* **2019**, *298*, 23–30.
- [20] (a) K. Kazimierczuk, J. Stanek, A. Zawadzka-Kazimierczuk, W. Koźmiński, *Prog. Nucl. Magn. Reson. Spectrosc.* **2010**, *57*, 420–434; (b) M. Mobli, J. C. Hoch, *Prog. Nucl. Magn. Reson. Spectrosc.* **2014**, *83*, 21–41; (c) K. Kazimierczuk, V. Orekhov, *Magn. Reson. Chem.* **2015**, *53*, 921–926; (d) D. Gołowicz, P. Kasprzak, V. Orekhov, K. Kazimierczuk, *Prog. Nucl. Magn. Reson. Spectrosc.* **2020**, *116*, 40–55.

Supporting Information
for
Diversifying NMR Supersequences with New
HSQC-based Modules

Jonathan R. J. Yong,¹ Alexandar L. Hansen,² Ēriks Kupče,³ Tim D. W.
Claridge^{1,*}

¹ *Chemistry Research Laboratory, Department of Chemistry, University of Oxford,
Mansfield Road, Oxford, OX1 3TA, U.K.*

² *Campus Chemical Instrument Center, The Ohio State University, 460 W. 12th Avenue,
Columbus, OH, 43210 U.S.*

³ *Bruker UK Ltd., Banner Lane, Coventry, CV4 9GH, U.K.*

* tim.claridge@chem.ox.ac.uk

Contents

1 Product operator analysis for pulse sequences	S3
2 Origin and suppression of wing artefacts	S4
3 Effect of setting $\Delta' = 1/(4 \cdot {}^1J_{\text{CH}})$ in seHSQC	S8
4 Comparison of BIG-BIRD and ZIP elements	S10
5 Multiplicity editing in seHSQC	S11
6 Summary of ${}^{13}\text{C}$ seHSQC sensitivity comparisons	S12
7 Retention of bulk magnetisation by ${}^{15}\text{N}$ modules	S14
8 ${}^{15}\text{N}$ HSQC and line broadening	S15
9 Effect of lengthened gradients in ${}^{15}\text{N}$ modules	S16
10 Sensitivity and resolution in ${}^{15}\text{N}$ modules	S17
10.1 Overview	S17
10.2 Default processing	S17
10.3 Extra linear prediction	S18
10.4 Discussion	S18
11 HSQC-TOCSY/HSQC sensitivity comparisons	S24
12 Other example spectra	S28
13 Sensitivity per unit time gains	S31
References	S33

1 Product operator analysis for pulse sequences

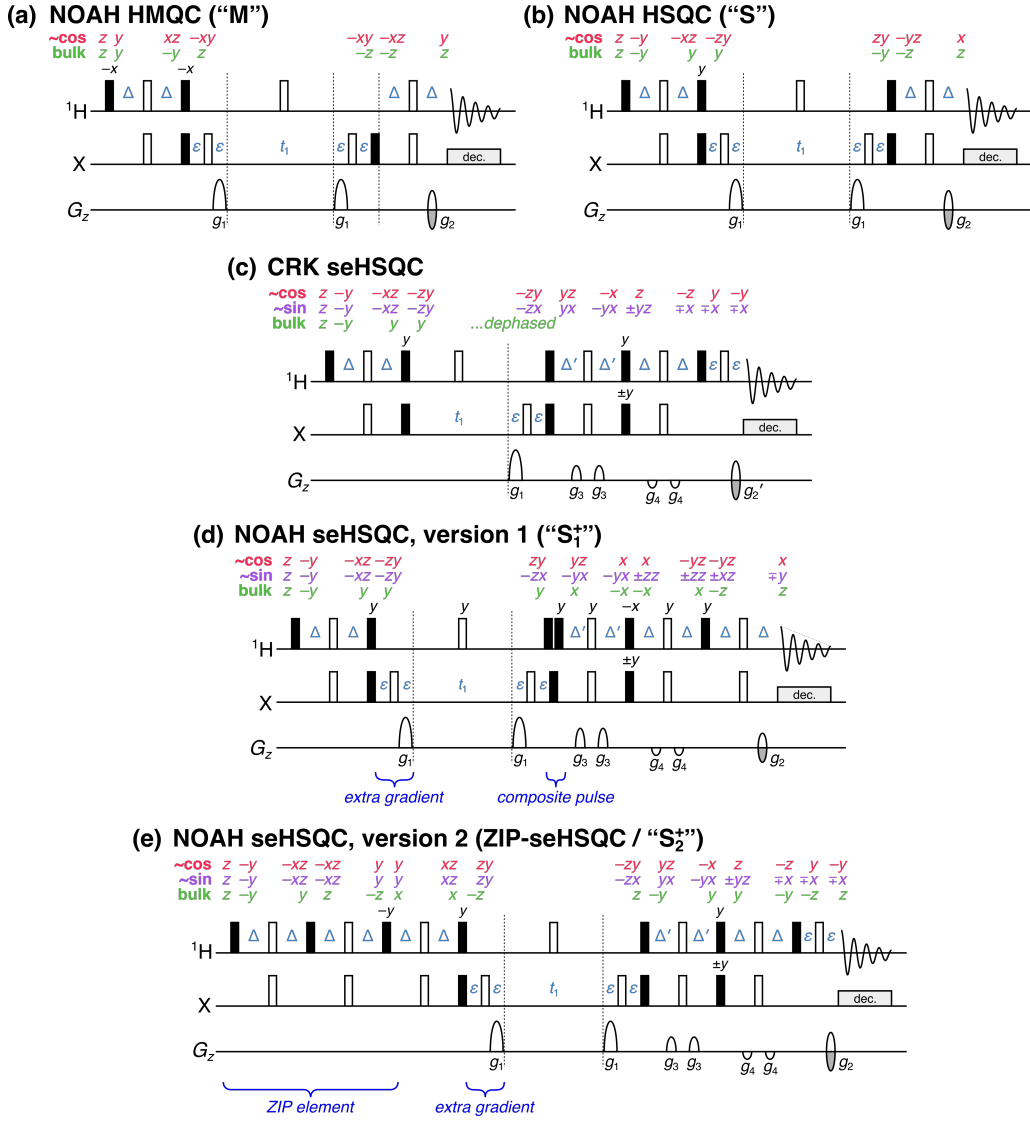


Figure S1: Product operators for an IS spin system at each stage of the HSQC and seHSQC sequences described in the main text. One-letter terms m ($m \in \{x, y, z\}$) are shorthand for single-spin terms on proton, i.e. \hat{I}_m . Two-letter terms mn are shorthand for two-spin terms on both the proton and heteronucleus, i.e. $2\hat{I}_m\hat{S}_n$. “~cos” represents the pathway for ${}^1\text{H}^{\text{C}}$ magnetisation that is cosine-modulated after t_1 : for the HMQC and HSQC, this is the only component that is detected. For the seHSQC, the sine-modulated ${}^1\text{H}^{\text{C}}$ component (labelled with “~sin”) is also detected. “bulk” refers to the bulk ${}^1\text{H}^{\text{C}}$ magnetisation, i.e. protons that are not directly coupled to the heteronucleus. Note that this analysis assumes $\Delta = \Delta' = 1/(4 \cdot {}^1J_{\text{XH}})$. All other symbols have the same meaning as in Figure 1 of the main text. (a) NOAH HMQC (“M”). (b) NOAH HSQC (“S”). (c) Cavanagh–Rance–Kay seHSQC; notice that the bulk magnetisation is dephased by the lone t_1 gradient. (d) NOAH seHSQC, version 1 (“S₁⁺”). (e) NOAH seHSQC, version 2 (“S₂⁺”). Immediately following the ZIP pulse sequence element, directly bonded protons are rotated onto $+y$, whereas the bulk magnetisation is rotated onto $+x$.

2 Origin and suppression of wing artefacts

The origin of the “wing” artefacts in the final homonuclear modules can be most clearly seen from the following series of experiments involving the NOAH-3 ^{15}N seHSQC/ ^{13}C ZIP-seHSQC/CLIP-COSY ($\text{S}_\text{N}^+\text{S}_2^+\text{C}^\text{c}$) supersequence. As described in the main text, if the extra gradient before t_1 is not present, each peak in the COSY with an indirect-dimension frequency of $f_1 = \Omega_\text{H}$ is flanked by a pair of artefacts at

$$f_1 = \Omega_\text{H} \pm \Omega_\text{H} \cdot \left(\frac{\text{SW}_{\text{COSY}}}{2 \cdot \text{SW}_{\text{HSQC}}} \right),$$

where Ω_H is the offset of the relevant proton and SW refers to the indirect-dimension spectral width. Since the f_1 spectral widths of the two seHSQC modules are different, they lead to distinct sets of wing artefacts in the COSY. In the spectra shown in the following figures, we have

$$\begin{aligned} \text{SW}_{^{15}\text{N HSQC}} &= 2128 \text{ Hz} \\ \text{SW}_{^{13}\text{C HSQC}} &= 23810 \text{ Hz} \\ \text{SW}_{\text{COSY}} &= 8418 \text{ Hz} \end{aligned}$$

meaning that the artefacts coming from the ^{15}N seHSQC occur at $f_1 = (1.00 \pm 1.98)\Omega_\text{H}$ (and are therefore often folded), whereas artefacts coming from the ^{13}C seHSQC occur at $f_1 = (1.00 \pm 0.18)\Omega_\text{H}$ (and are typically found very close to the main peak). In both cases, the artefacts associated with intense methyl group peaks are the most obvious, but similar artefacts are observed for all other peaks, albeit with lower absolute intensities.

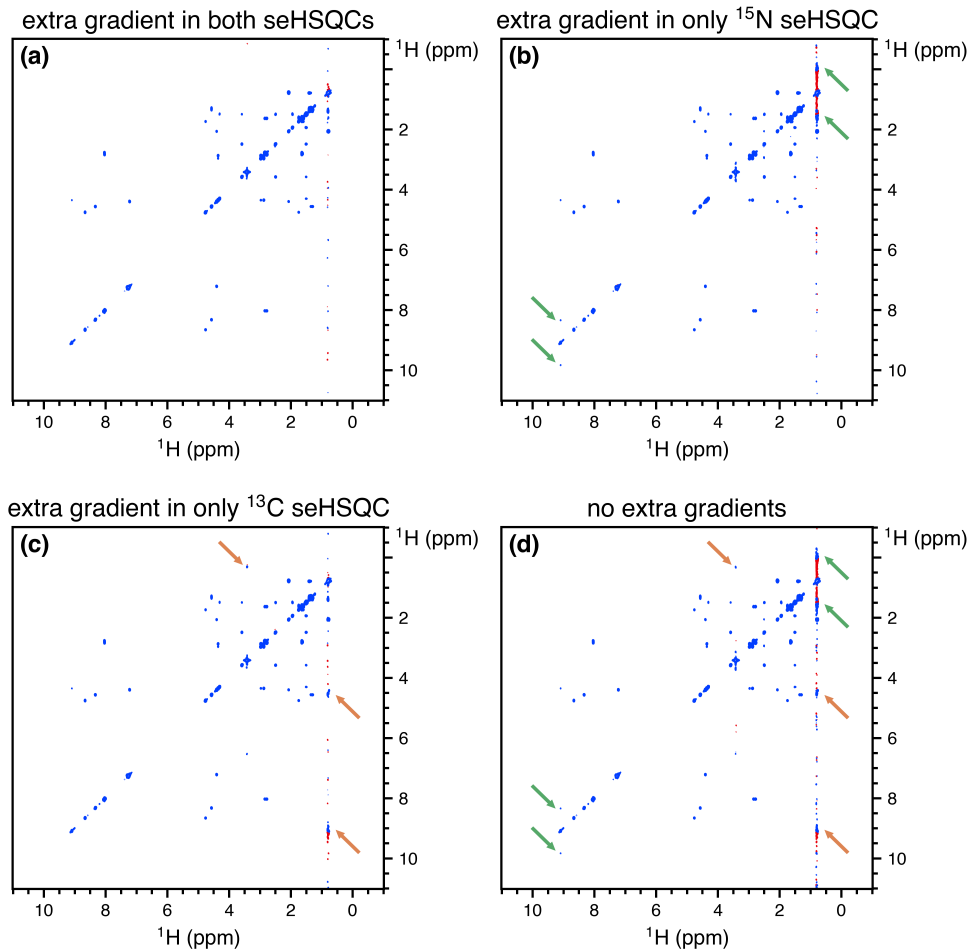


Figure S2: CLIP-COSY spectra obtained from various forms of the NOAH-3 $S_N^+S_2^+C^c$ supersequence. Wing artefacts arising from the ^{15}N seHSQC are highlighted in orange; those arising from the ^{13}C seHSQC in green. Notice how (in this case) the former can easily be misinterpreted as a crosspeak, while the latter obscures genuine crosspeaks. **(a)** With the extra gradient inserted for both modules, i.e. no artefacts. **(b)** With an extra gradient in only the ^{15}N module, i.e. only the ^{13}C artefacts. **(c)** With an extra gradient in only the ^{13}C module. **(d)** With no extra gradients. Spectra were obtained on a 700 MHz Bruker AV III equipped with a TCI H/C/N cryoprobe; the sample used was 40 mM gramicidin in $\text{DMSO}-d_6$.

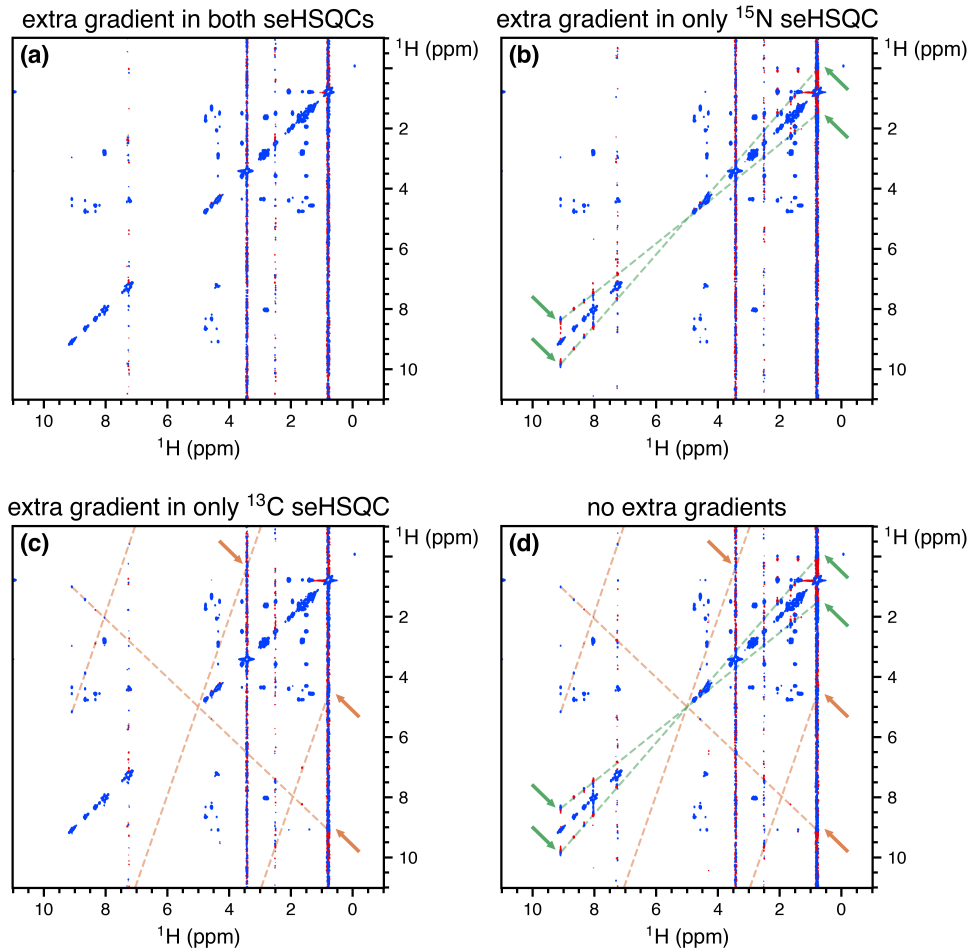


Figure S3: The same spectra as Figure S2, but plotted with a smaller base contour level to illustrate the regular indirect-dimension frequencies of the wing artefacts. A greater number of artefacts are now visible (in addition to those already highlighted in Figure S2, which are still marked with arrows). The artefacts arising from the ^{15}N seHSQC lie on the orange dotted line; those arising from the ^{13}C seHSQC lie on the green dotted line. **(a)** With the extra gradient inserted for both modules, i.e. no artefacts. **(b)** With an extra gradient in only the ^{15}N module, i.e. only the ^{13}C artefacts. **(c)** With an extra gradient in only the ^{13}C module. **(d)** With no extra gradients. Spectra were obtained on a 700 MHz Bruker AV III equipped with a TCI H/C/N cryoprobe; the sample used was 40 mM gramicidin in DMSO- d_6 .

Additional information can be gleaned from the following series of CLIP-COSY spectra, obtained from NOAH-2 $S_2^+ C^c$ supersequences. In the seHSQC module, the two gradients g_1 in the t_1 period are independently enabled or disabled (by setting their amplitude to 0). Traces of the resulting CLIP-COSY spectra are shown in Figure S4. The gradients serve to dephase any bulk $^1H^{13}C$ magnetisation that is transverse during either half of t_1 : therefore, if (for example) the gradient in the first half of t_1 is switched off, this allows bulk magnetisation that is transverse in the first half of t_1 to evolve and ultimately contribute to the wing artefacts in the CLIP-COSY. As can be seen, gradients must be applied in *both* halves for complete suppression of the wing artefacts.

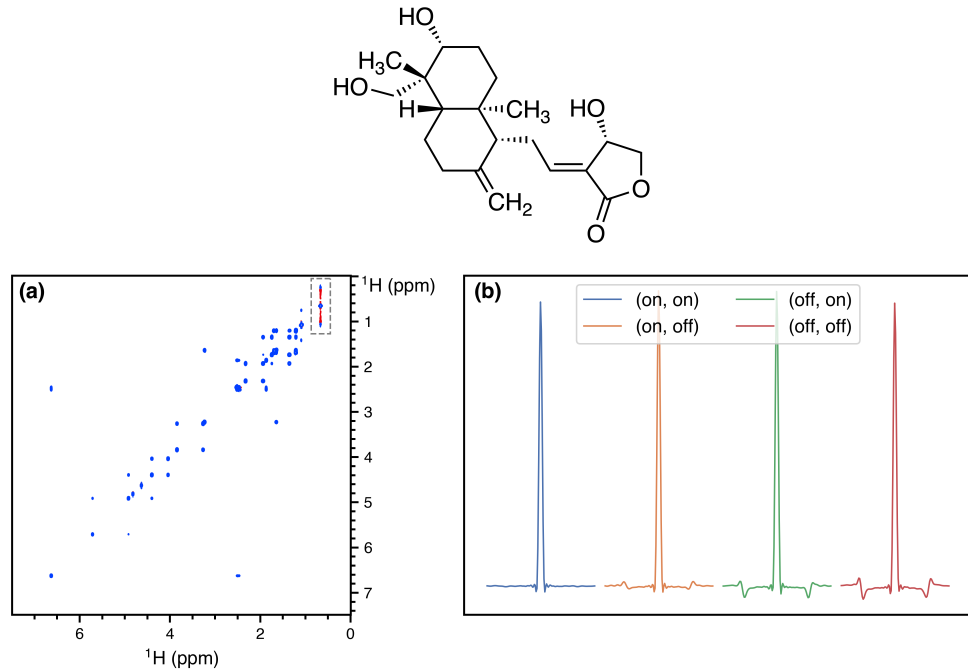


Figure S4: (a) CLIP-COSY spectrum obtained from NOAH-2 $S_2^+ C^c$ sequence, where both gradients in t_1 were disabled (i.e. “(off, off)”). The other three CLIP-COSY spectra are similar, except that the (on, on) spectrum (with gradients applied in both halves of t_1) does not have wing artefacts (grey box). (b) f_1 traces through 0.67 ppm of the four CLIP-COSY spectra obtained with various combinations of gradients, corresponding to the boxed area in (a). Only the (on, on) spectrum (in blue) is free from wing artefacts. The (on, off) and (off, on) spectra (in orange and green respectively) have wing artefacts arising from bulk magnetisation that evolves during the second and first halves of the seHSQC t_1 period respectively. The (off, off) spectrum (red), which corresponds to the 2D spectrum in (a), has the greatest intensity of wing artefacts. Spectra were obtained on a 700 MHz Bruker AV III equipped with a TCI H/C/N cryoprobe; the sample used was 40 mM andrographolide in $DMSO-d_6$.

It is interesting to note that the evolution of magnetisation during multiple indirect dimensions is the basis of projection spectroscopy,^[1] where the resulting sums and differences of frequencies can be used to reconstruct higher-dimensional spectra. In the present context, the aim is instead to suppress these peaks, permitting evolution to only occur in a single indirect dimension.

3 Effect of setting $\Delta' = 1/(4 \cdot {}^1J_{CH})$ in seHSQC

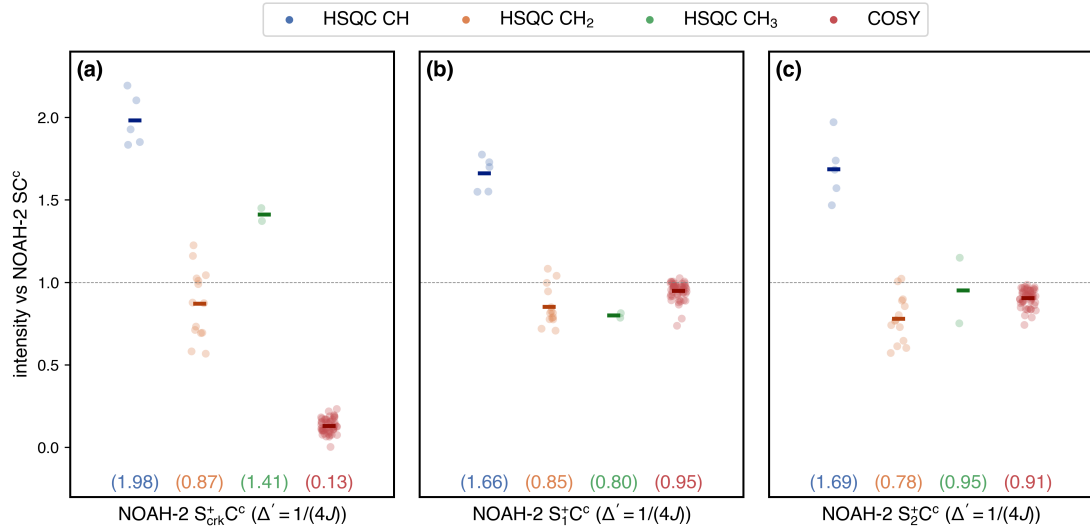


Figure S5: Sensitivity of NOAH-2 $S^+ C^c$ supersequences with Δ' set to $1/(4 \cdot {}^1J_{CH})$, relative to the NOAH-2 SC^c supersequence. (a) Using the CRK seHSQC. (b) Using the S_1^+ module. (c) Using the S_2^+ module. Spectra were obtained on a 700 MHz Bruker AV III equipped with a TCI H/C/N cryoprobe; the sample used was 40 mM andrographolide in $DMSO-d_6$.

By setting $\Delta' = 1/(4 \cdot {}^1J_{CH})$, theory predicts a larger sensitivity enhancement for CH peaks, whereas CH_2 and CH_3 peaks should have sensitivities comparable to the unenhanced HSQC.

Although the CRK seHSQC has slightly better performance over the NOAH seHSQCs, its major drawback remains in that it does not preserve any ${}^1H^{IX}$ magnetisation for a subsequent homonuclear module (Figure S5a): the duration of Δ' chosen does not affect this in any way. Thus, we limit our discussion to the two NOAH seHSQC variants (Figures S5b and S5c). Both of these do indeed display the expected gains for CH peaks: the corresponding sensitivities with $\Delta' = 1/(8 \cdot {}^1J_{CH})$ are shown in Figure 2. For CH_2 and CH_3 peaks, we observe sensitivity *losses* even relative to the unenhanced HSQC; this is likely due to pulse imperfections in the longer pulse sequence and is in line with previous studies.^[2] This is generally not desirable in a ${}^{13}C$ seHSQC, where CH_2 peaks are common and are often further split due to diastereotopicity. However, in the ${}^{15}N$ seHSQC, the delay Δ' can often be set to $1/(4 \cdot {}^1J_{NH})$ to provide the maximum sensitivity enhancement for NH peaks.

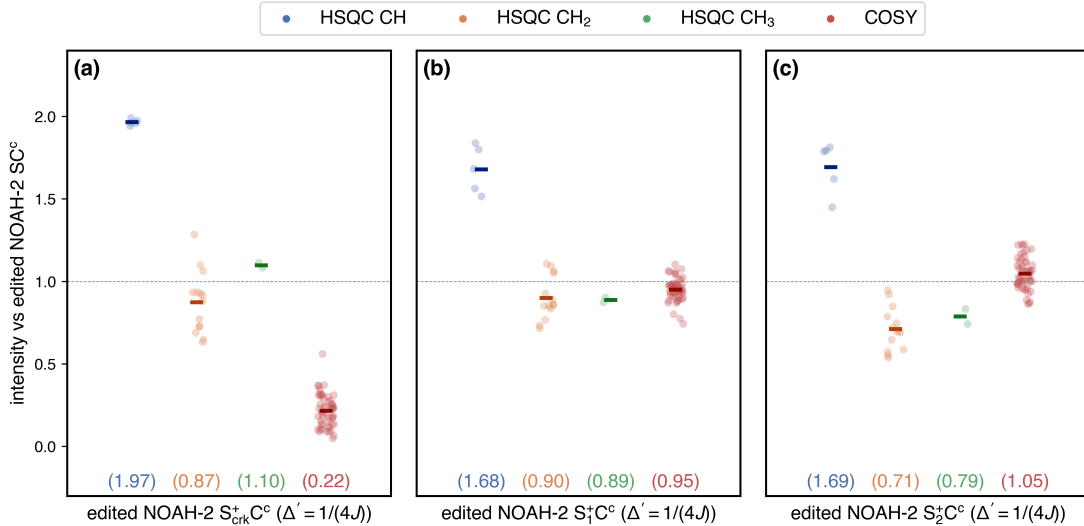


Figure S6: Sensitivity of multiplicity-edited NOAH-2 S^+C^c supersequences with Δ' set to $1/(4 \cdot {}^1J_{CH})$, relative to the multiplicity-edited NOAH-2 SC^c supersequence. (a) Using the CRK seHSQC. (b) Using the S_1^+ module. (c) Using the S_2^+ module. Spectra were obtained on a 700 MHz Bruker AV III equipped with a TCI H/C/N cryoprobe; the sample used was 40 mM andrographolide in DMSO-*d*₆.

The inclusion of multiplicity editing in the sequences with $\Delta' = 1/(4 \cdot {}^1J_{CH})$ makes no substantial difference to the results (Figure S6), save for a slight relative improvement in the amount of ${}^1H^{IX}$ magnetisation preserved by the S_2^+ module. The reasons for this are discussed in the main text.

4 Comparison of BIG-BIRD and ZIP elements

The BIG-BIRD element used here was $45^\circ_{45^\circ}(^1\text{H}) - 2\Delta - 180^\circ(^1\text{H}, ^{13}\text{C}) - 2\Delta - 45^\circ_{225^\circ}(^1\text{H})$ for the unedited NOAH seHSQC, where β_ϕ indicates a hard pulse with flip angle β and phase ϕ , and $\Delta = 1/(4 \cdot ^1J_{\text{CH}})$. For the edited NOAH seHSQC, the BIG-BIRD pulse phases are slightly modified to give $45^\circ_{315^\circ}(^1\text{H}) - 2\Delta - 180^\circ(^1\text{H}, ^{13}\text{C}) - 2\Delta - 45^\circ_{135^\circ}(^1\text{H})$. These, and the ZIP, have the same net effect on $^1\text{H}^{\text{C}}$ and $^1\text{H}^{!C}$ magnetisation, as can be seen from the product operator analysis in Figure S1. Thus, they can be used interchangeably in version 2 of the NOAH seHSQC. However, the ZIP provides greater sensitivity in both the HSQC and downstream COSY (Figure S7).

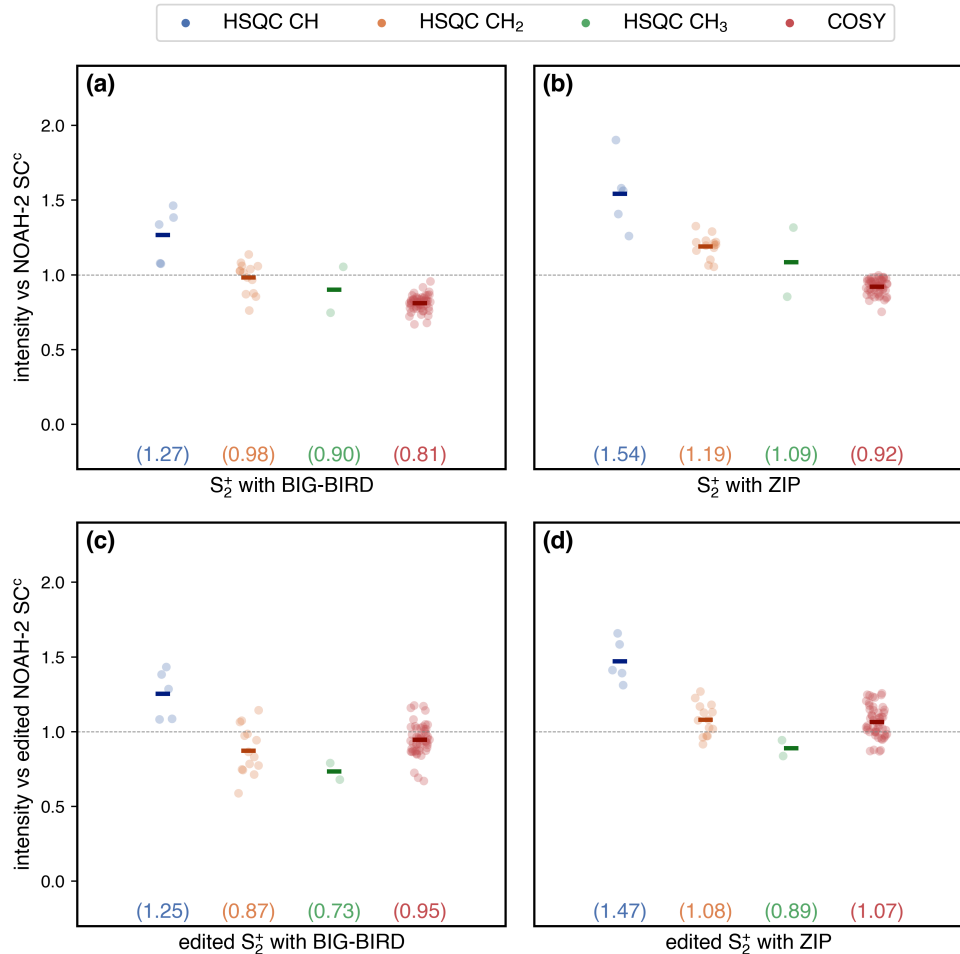


Figure S7: Sensitivity of NOAH-2 $S_2^+ \text{C}^{\text{c}}$ supersequences with either BIG-BIRD or ZIP elements, versus the corresponding NOAH-2 SC^{c} supersequences (i.e. unedited for (a) and (b), edited for (c) and (d)). The value of Δ' was set to $1/(8 \cdot ^1J_{\text{CH}})$. (a) Using the unedited NOAH seHSQC with the BIG-BIRD element. (b) Unedited seHSQC with ZIP. (c) Edited seHSQC with BIG-BIRD. (d) Edited seHSQC with ZIP. Spectra were obtained on a 700 MHz Bruker AV III equipped with a TCI H/C/N cryoprobe; the sample used was 40 mM andrographolide in DMSO-*d*₆.

5 Multiplicity editing in seHSQC

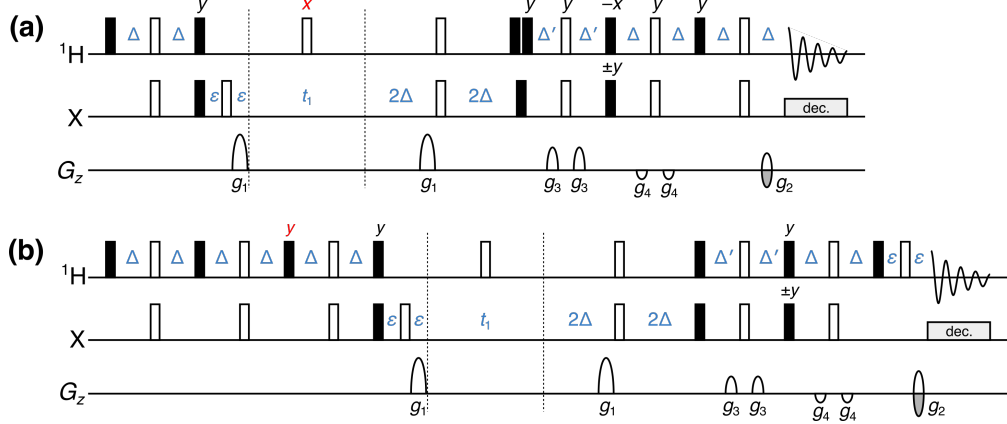


Figure S8: Implementation of multiplicity editing in the new NOAH seHSQC modules. Pulse phases which differ from the unedited versions (Figure S1) are highlighted in red; these are needed to compensate for the extra ¹H 180° pulse in the editing period. Symbols have the same meaning as in Figure 1 of the main text. (a) NOAH seHSQC, version 1 ("S₁⁺"). (b) NOAH seHSQC, version 2 ("S₂⁺").

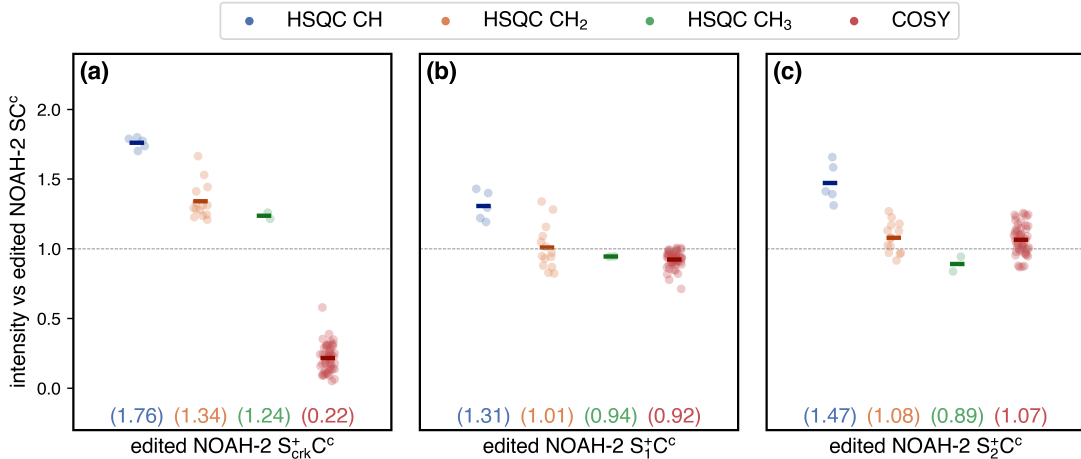


Figure S9: Sensitivity of multiplicity-edited S⁺C^c supersequences, relative to the SC^c supersequence. Spectra were obtained with $\Delta' = 1/(8 \cdot ^1J_{CH})$. (a) Using the CRK seHSQC. (b) Using the S₁⁺ module. (c) Using the S₂⁺ module. Spectra were obtained on a 700 MHz Bruker AV III equipped with a TCI H/C/N cryoprobe; the sample used was 40 mM andrographolide in DMSO-*d*₆.

On average, both versions of the NOAH seHSQC provide sensitivity gains for HSQC CH and CH₂ peaks (Figures S9b and S9c) while not compromising the COSY intensities as the CRK seHSQC does (Figure S9a). The S₂⁺ module in particular provides slightly better performance. Note also how the COSY intensities with the S₂⁺ module are on average higher than with the original HSQC module: this indicates that the S₂⁺ module preserves bulk ¹H/¹³C magnetisation better. As discussed in the main text, this is because the bulk magnetisation is longitudinal during the editing period.

6 Summary of ^{13}C seHSQC sensitivity comparisons

Experiment		HSQC			COSY	Figure	
edited?	HSQC variant	Δ'	CH	CH_2	CH_3		
no	HSQC	–	1.00*	1.00*	1.00*	1.00*	–
	CRK seHSQC	1/(8J)	1.80	1.32	1.58	0.13	2b
	NOAH seHSQC v1	1/(8J)	1.29	0.94	0.89	0.94	2c
	NOAH seHSQC v2	1/(8J)	1.54	1.19	1.09	0.92	2d
	CRK seHSQC	1/(4J)	1.98	0.87	1.41	0.13	S5a
	NOAH seHSQC v1	1/(4J)	1.66	0.85	0.80	0.95	S5b
	NOAH seHSQC v2	1/(4J)	1.69	0.78	0.95	0.91	S5c
	no HSQC, only COSY	–	–	–	–	1.09	–
yes	HSQC	–	1.00†	1.00†	1.00†	1.00†	–
	CRK seHSQC	1/(8J)	1.76	1.34	1.24	0.22	S9a
	NOAH seHSQC v1	1/(8J)	1.31	1.01	0.94	0.92	S9b
	NOAH seHSQC v2	1/(8J)	1.47	1.08	0.89	1.07	S9c
	CRK seHSQC	1/(4J)	1.97	0.87	1.10	0.22	S6a
	NOAH seHSQC v1	1/(4J)	1.68	0.90	0.89	0.95	S6b
	NOAH seHSQC v2	1/(4J)	1.69	0.71	0.79	1.05	S6c
	no HSQC, only COSY	–	–	–	–	1.29	–

Table S1: Relative sensitivities of HSQC and CLIP-COSY spectra in NOAH-2 SC^c and S⁺C^c supersequences. All sensitivities are normalised against the corresponding SC^c sequences: in particular, the unedited seHSQC supersequences are compared against the unedited SC^c (marked with *), and likewise edited seHSQC supersequences are compared against the edited SC^c (marked with †). Note that the two standalone CLIP-COSY entries (the last row in both sections) refer to the same spectrum, and therefore have the same *absolute* sensitivity. The difference in the *relative* sensitivity arises only because they are being compared against the COSY intensities in different reference supersequences, which is done here for consistency with the other figures in this text. See Table S2 for a version of this table where the COSY sensitivities in both unedited and edited supersequences are normalised against the standalone CLIP-COSY. Spectra were obtained on a 700 MHz Bruker AV III equipped with a TCI H/C/N cryoprobe; the sample used was 40 mM andrographolide in DMSO-*d*₆.

edited?	HSQC variant	Δ'	HSQC			COSY
			CH	CH ₂	CH ₃	
no	HSQC	–	1.00*	1.00*	1.00*	0.93
	CRK seHSQC	1/(8J)	1.80	1.32	1.58	0.12
	NOAH seHSQC v1	1/(8J)	1.29	0.94	0.89	0.88
	NOAH seHSQC v2	1/(8J)	1.54	1.19	1.09	0.85
	CRK seHSQC	1/(4J)	1.98	0.87	1.41	0.12
	NOAH seHSQC v1	1/(4J)	1.66	0.85	0.80	0.88
	NOAH seHSQC v2	1/(4J)	1.69	0.78	0.95	0.84
	no HSQC, only COSY	–	–	–	–	1.00‡
yes	HSQC	–	1.00†	1.00†	1.00†	0.79
	CRK seHSQC	1/(8J)	1.76	1.34	1.24	0.17
	NOAH seHSQC v1	1/(8J)	1.31	1.01	0.94	0.73
	NOAH seHSQC v2	1/(8J)	1.47	1.08	0.89	0.84
	CRK seHSQC	1/(4J)	1.97	0.87	1.10	0.17
	NOAH seHSQC v1	1/(4J)	1.68	0.90	0.89	0.75
	NOAH seHSQC v2	1/(4J)	1.69	0.71	0.79	0.82
	no HSQC, only COSY	–	–	–	–	1.00‡

Table S2: Relative sensitivities of HSQC and CLIP-COSY spectra in NOAH-2 SC^c and S⁺C^c supersequences. All HSQC sensitivities are normalised against the HSQC spectrum in the corresponding SC^c sequences: in particular, the unedited seHSQCs are compared against the unedited HSQC (marked with *), and likewise edited seHSQCs are compared against the edited HSQC (marked with †). All COSY sensitivities are compared against the standalone CLIP-COSY spectrum (the last row in both sections, marked with ‡). This is different from the figures used in this text, which compare the COSY intensities against the COSY component of the corresponding SC^c supersequence. See Table S1 for a version of this table which is consistent with the other figures in this text. Spectra were obtained on a 700 MHz Bruker AV III equipped with a TCI H/C/N cryoprobe; the sample used was 40 mM andrographolide in DMSO-*d*₆.

7 Retention of bulk magnetisation by ^{15}N modules

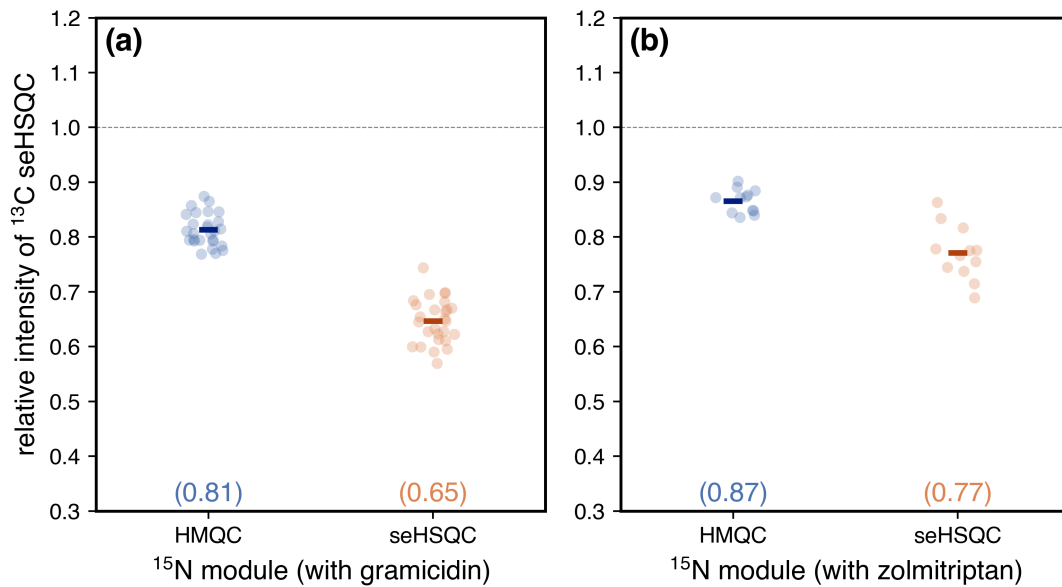


Figure S10: Signal intensities of the ^{13}C seHSQC in NOAH-3 $\text{XS}_2^+ \text{C}^\text{c}$ supersequences, normalised against a reference ^{13}C seHSQC taken from a NOAH-2 $\text{S}_2^+ \text{C}^\text{c}$ supersequence. The module X is either the ^{15}N HMQC (M) or the ^{15}N seHSQC (S_N^+); the numbers indicate the amount of $^{1\text{H}}\text{C}$ magnetisation that is preserved by the ^{15}N module. **(a)** Using 40 mM gramicidin in $\text{DMSO}-d_6$. **(b)** Using 50 mM zolmitriptan in $\text{DMSO}-d_6$. Spectra were obtained on a 700 MHz Bruker AV III equipped with a TCI H/C/N cryoprobe.

8 ^{15}N HSQC and line broadening

For $^{15}\text{N}-^1\text{H}$ correlations, both the HMQC and version 2 of the new seHSQC are recommended as they keep the bulk magnetisation (both $^1\text{H}^{\text{C}}$ and $^1\text{H}^{\text{IX}}$) along $\pm z$ during the t_1 period. The HSQC module, as well as version 1 of the seHSQC, place this magnetisation in the xy -plane during t_1 , leading to J_{HH} evolution; consequently, the amount of bulk magnetisation “passed on” to the downstream modules decreases as the ^{15}N t_1 is increased. Since t_1 for each NOAH module is incremented in sync, this is manifested in downstream modules as a t_1 -dependent decrease in amplitude, or f_1 line broadening after Fourier transformation, as shown in Figure S11.

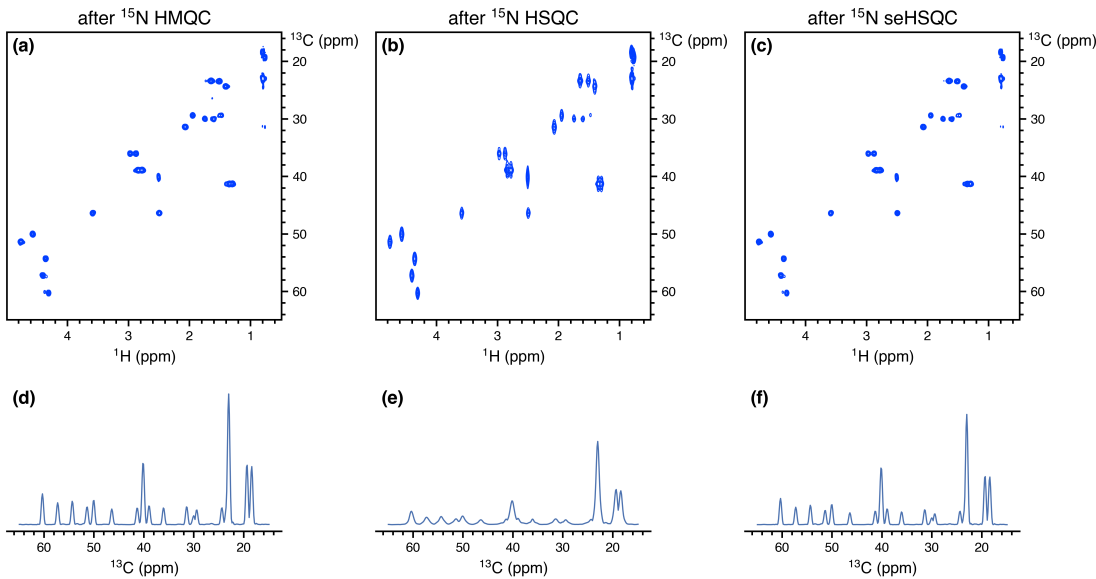


Figure S11: ^{13}C seHSQC spectra obtained from NOAH-3 $\text{XS}_2^+ \text{C}^{\text{c}}$ (^{15}N module + ^{13}C seHSQC + CLIP-COSY) supersequences. The ^{15}N spectral width was 30 ppm and 256 t_1 increments were collected, corresponding to an indirect-dimension ^{15}N acquisition time of 60.1 ms. (a) X = HMQC (“M”). (b) X = HSQC (“S”). (c) X = seHSQC (“ S_N^+ ”). (d)–(f) Projections of spectra (a)–(c) onto the f_1 axis. Note the f_1 line broadening in (b) and (e). Spectra were obtained on a 700 MHz Bruker AV III equipped with a TCI H/C/N cryoprobe; the sample used was 40 mM gramicidin in $\text{DMSO}-d_6$.

This line broadening also leads to a substantial sensitivity loss (for example, across all peaks, the ^{13}C seHSQC in Figure S11b has almost 65% lower sensitivity than that in Figure S11a). The extent of the line broadening depends on the acquisition time (AQ), and is particularly pronounced for long acquisition times, i.e. small ^{15}N spectral widths. Thus, the effect may be mitigated by reducing AQ, for example by using k -scaling: indeed, the 60.1 ms used in Figure S11 to illustrate the effect is often not necessary for ^{15}N spectra. However, even at an AQ of 15.0 ms (i.e. $k = 4$), there is still discernible broadening which leads to a 25% loss of sensitivity. Of course, this issue can be entirely avoided by using either the HMQC or seHSQC.

9 Effect of lengthened gradients in ^{15}N modules

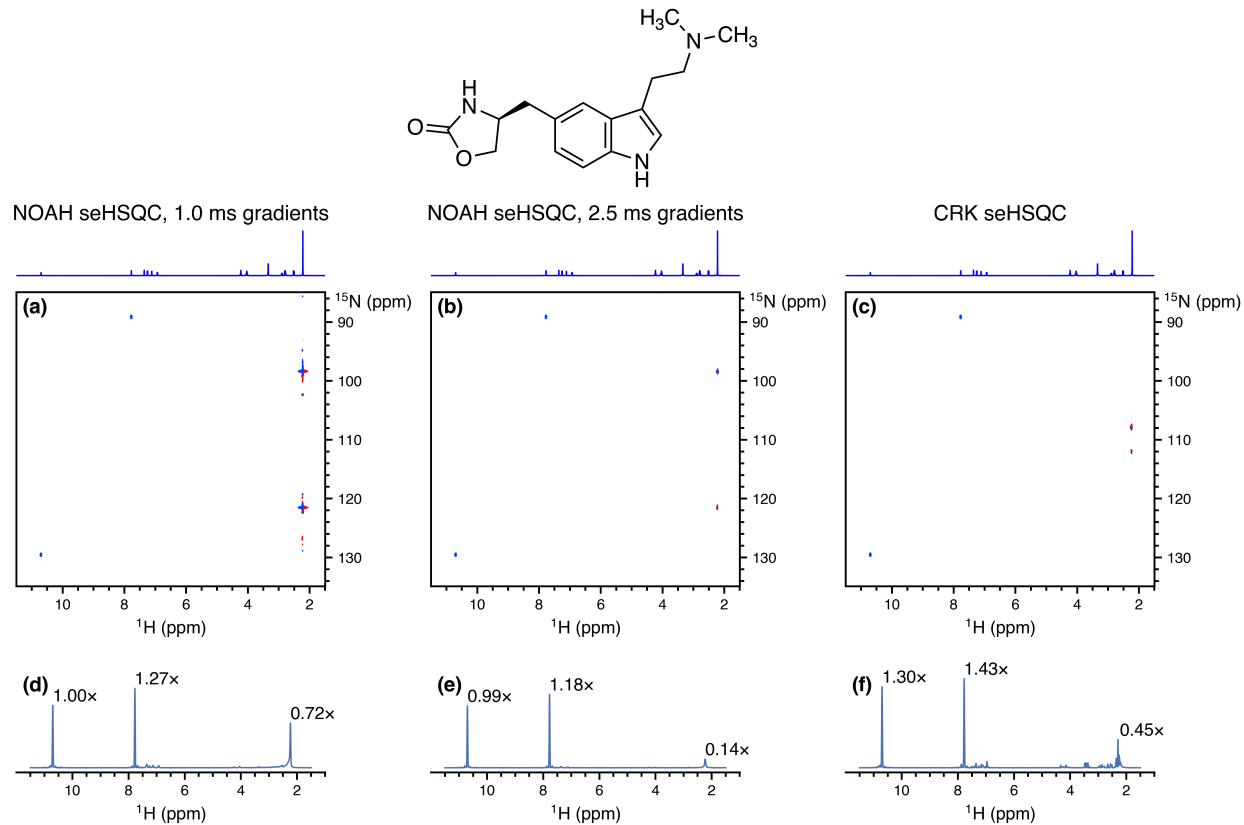


Figure S12: ^{15}N seHSQC spectra obtained using the NOAH and CRK implementations. The peaks at 7.8 and 10.7 ppm (^1H shifts) are genuine crosspeaks; the mixed-phase peaks at 2.2 ppm are artefacts. The 1D ^1H spectrum is shown above each of the 2D spectra in (a)–(c); the artefacts seen in the 2D correspond to the intense N -methyl groups at 2.2 ppm. (a) NOAH seHSQC, with original CTP gradients of 1 ms. (b) NOAH seHSQC, with longer CTP gradients of 1 ms. (c) Standalone CRK seHSQC with 1 ms CTP gradients (Bruker `hsqcetf3gpsi2` pulse programme). (d)–(f) Projections of spectra (a)–(c) onto the f_2 axis. The numbers indicate relative peak heights (normalised against the 10.7 ppm peak in (d)). Spectra were obtained on a 700 MHz Bruker AV III equipped with a TCI H/C/N cryoprobe; the sample used was 50 mM zolmitriptan in $\text{DMSO}-d_6$.

The lengthening of CTP gradients from 1 ms to 2.5 ms is aimed at cleaning up artefacts arising from bulk magnetisation that is not properly returned to $+z$ at the end of the sequence. Figure S12 shows exactly how effective this strategy is. In (d), where the CTP gradients have their original duration, the artefacts originating from the intense methyl groups have comparable intensity to the desired peaks. When the gradients are lengthened in (e), the crosspeak intensities are almost unaffected, whereas the artefacts are suppressed by a factor of 5 or more. Although this suppression is not complete, this should not be interpreted as a weakness of the new NOAH seHSQC module, as similar artefacts are also visible in the CRK seHSQC (f). Indeed, every ^{15}N – ^1H experiment we tested has at least *some* artefact intensity in this region.

10 Sensitivity and resolution in ^{15}N modules

10.1 Overview

In ideal cases, it is possible to modify the acquisition scheme of a 2D experiment, such that resolution in the indirect dimension is decreased in return for gains in sensitivity: this has previously been illustrated in the context of time-shared $^{15}\text{N},^{13}\text{C}$ HMBC spectra.^[3,4] This can prove to be useful particularly in ^{15}N modules, where the number of peaks is typically small, and are well-dispersed across the chemical shift range (thus minimising the chances of accidental overlap). The key parameter here is the indirect-dimension acquisition time (AQ): a shorter AQ leads to poorer resolution but higher sensitivity (ideally). We propose two different, but ultimately very similar, methods of reducing AQ:

1. *k*-scaling: decreasing the number of t_1 increments (TD1) by a factor of k leads to a decrease in AQ by a factor of k . In its place, the number of scans (NS) can be increased by a factor of k .
2. SW-scaling: increasing the indirect-dimension spectral width (SW) by a factor of k (but leaving TD1 and NS unchanged) leads to an equivalent decrease in AQ.

These possibilities are illustrated schematically in Figure S13. The “standard” experiment (Figure S13a) is acquired as described in the *Experimental* section of the main text, i.e. TD1 = 256, NS = 2, and SW = 30 ppm (for gramicidin).

10.2 Default processing

For both the *k*- and SW-scaled spectra, the entries that are *not* marked “(+LP)” utilise default TopSpin processing parameters, which applies linear prediction of another TD1 points beyond the original TD1 acquired points. This leads to an *effective acquisition time*, AQ_{eff}, which is double the original acquisition time AQ. In practice, the indirect-dimension resolution is not determined by AQ but rather AQ_{eff}: however, when the default processing is used, AQ_{eff} is itself proportional to AQ, and therefore resolution remains proportional to AQ.

The results of *k*- and SW-scaling are illustrated in Figures S14 and S15 for ^{15}N HMQC and seHSQC spectra respectively. By decreasing the indirect dimension resolution, the f_1 linewidths of the peaks increase: this can lead to significant sensitivity enhancement for the HMQC (up to 2.6×), because J_{HH} splitting in the f_1 dimension is no longer resolved. The largest gains are observed for peaks where J_{HH} splitting is better resolved; for the leftmost peak at $\delta_{\text{N}} = 128$ ppm which has no resolved J_{HH} splitting, only a more modest 1.7× gain in sensitivity is attained. For the seHSQC module, *k*-scaling on its own leads to far smaller sensitivity gains (Figure S15). Any increase in the total peak volume is almost completely offset by the f_1 broadening. Therefore, even at $k = 8$, the largest

sensitivity gains that can be attained are $\sim 1.3 \times$.

10.3 Extra linear prediction

It is clear, however, that AQ_{eff} can be arbitrarily extended by applying more extensive linear prediction: this is the case for the experiments in Figure S13a marked with “(+LP)”. In each case, we have applied linear prediction up to the original AQ_{eff} of 120.3 ms in order to recover the resolution of the “standard” spectrum. Although this leads to larger increases in peak height or SNR (by virtue of the decreased linewidths), this does not necessarily represent a true “sensitivity gain” in terms of the ability to reveal weak peaks.^[5]

Aggressive linear prediction is less successful for the HMQC spectra (Figure S16): although raw gains in peak height can be observed for all values of k , there is a corresponding decrease in the spectral quality, as evidenced by the f_1 multiplet structure becoming increasingly distorted. On the other hand, linear prediction performs well for the seHSQC spectra (Figure S17), where there is no multiplet structure in f_1 .

10.4 Discussion

It is difficult to draw firm conclusions from the spectra shown here, but some general guidelines may be mentioned:

- The sensitivity gains obtained without extra linear prediction (Figures S14 and S15) are almost identical for both k - and SW-scaling.
- k -scaling appears to provide larger raw gains in peak height when extra linear prediction is applied (Figures S16 and S17), although the fidelity of the reconstruction at large values of k is questionable, particularly for the HMQC.
- k -scaling is currently not compatible with the use of non-uniform sampling (NUS) in the rest of the NOAH supersequence, because two distinct NUS schedules would have to be maintained in the pulse programme (one for the k -scaled module and one for the other modules). If NUS is desired, then SW-scaling is the only viable option.

It should also be noted that k -scaling is a special case of *undersampling*, where the sampling schedule is chosen to simply be the first $TD1/k$ points, and the remainder reconstructed via linear prediction. A possible alternative would be to choose a different (non-uniform) sampling schedule for the ^{15}N module to reduce the number of t_1 increments, and in turn increase NS; the missing increments may be reconstructed using a number of NUS algorithms. We briefly investigated this on the present sample, but did not see any noticeable differences as compared to k -scaling. However, it is possible that under different circumstances, *bona fide* sensitivity gains may be attained compared to the “standard” spectrum.^[5c,6]

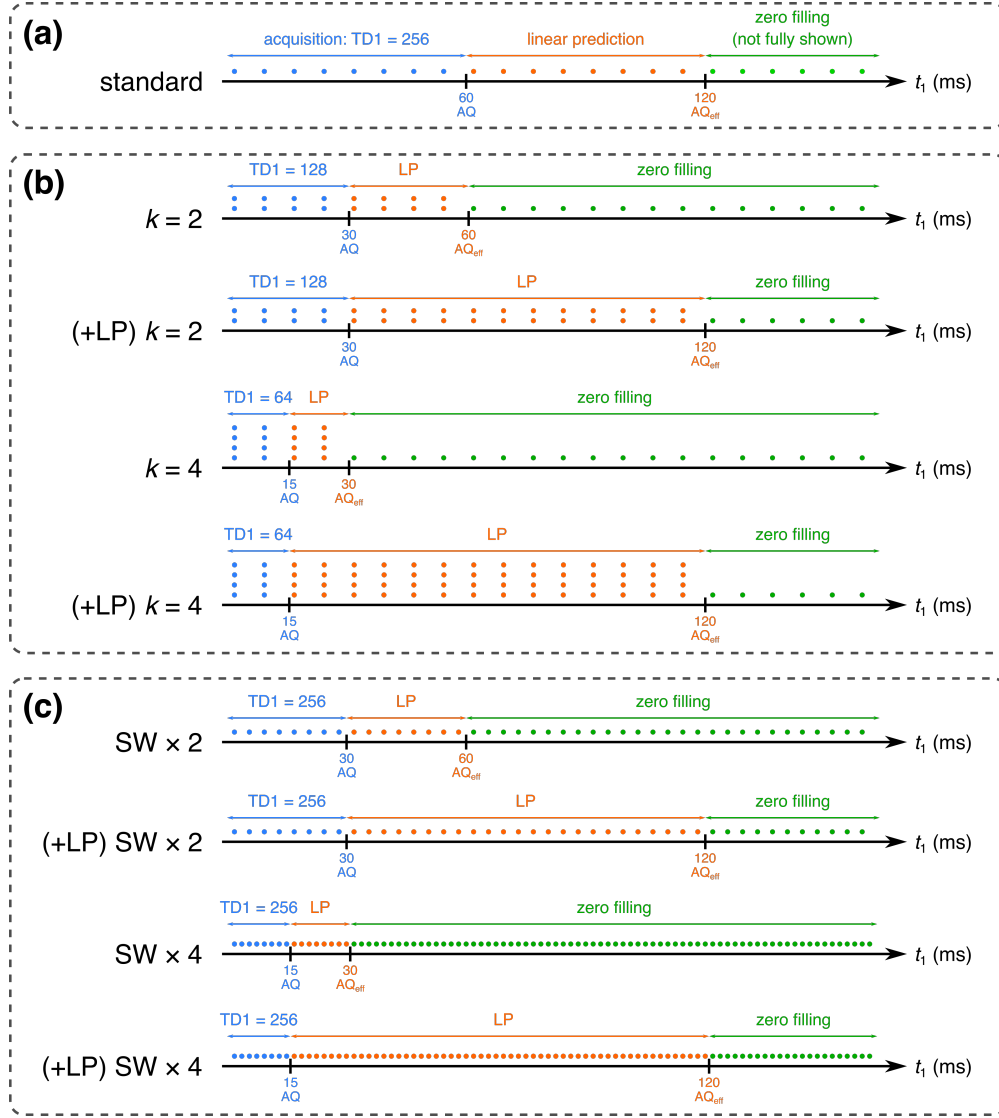


Figure S13: Pictorial representation of k - and SW-scaling, the two ways of reducing the indirect-dimension acquisition time discussed in the text. Each dot represents 32 t_1 increments with 2 scans per increment: blue dots indicate physically acquired data, orange dots indicate data constructed via forward linear prediction, and green dots indicate zeroes used to pad the FID in zero filling (not all zeroes are shown here). The total experimental time is proportional to the number of blue dots, and is kept constant in all of the above; the SNR is to a first approximation proportional to the square root of the number of blue and orange dots. The true indirect-dimension acquisition time (AQ), as well as an “effective” acquisition time obtained through linear prediction (AQ_{eff}), are indicated on the t_1 axis. The observed indirect-dimension resolution is directly proportional to AQ_{eff} . By default, TopSpin performs indirect-dimension linear prediction such that $AQ_{eff} = 2 \times AQ$; the rows marked “(+LP)” are experiments where extra linear prediction is applied to extend AQ_{eff} to the original value of 120.3 ms. (a) The “standard” experiment. (b) k -scaled experiments, where the number of t_1 increments (TD1) is reduced in favour of an increased number of scans (NS) per increment (symbolised by the vertically stacked dots). (c) SW-scaled experiments, where TD1 and NS remain unchanged, but the spacing between increments is decreased. Notice how AQ and AQ_{eff} are modified in exactly the same way as in (b). The effects of k - and SW-scaling are compared in Figures S14 to S17.

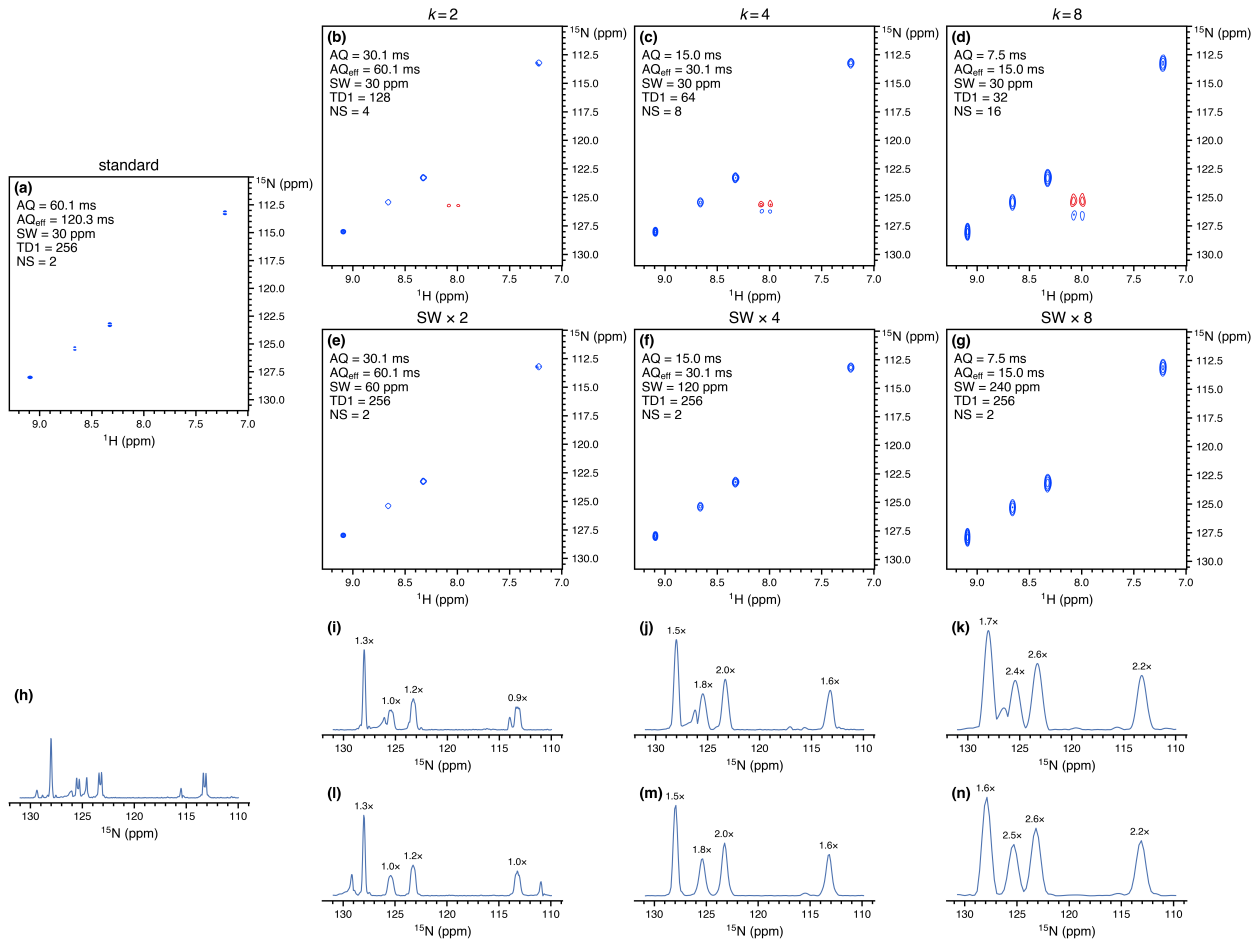


Figure S14: (HMQC without extra linear prediction.) ^{15}N HMQC spectra taken from NOAH-3 $\text{MS}_2^+ \text{C}^{\text{c}}$ supersequences. All spectra are plotted with the same noise levels. No linear prediction has been applied beyond the default processing in TopSpin; thus, AQ_{eff} is equal to $2 \times \text{AQ}$ for all of the spectra above. (a) The “standard” spectrum. (b) $k = 2$. (c) $k = 4$. (d) $k = 8$. (e) SW $\times 2$. (f) SW $\times 4$. (g) SW $\times 8$. (h)–(n) Projections of 2D spectra in (a)–(g) onto the f_1 axis. Numbers indicate peak heights relative to the “standard” HMQC spectrum in (a). The peak at $\delta_{\text{H}} = 8.03$ ppm is folded and therefore does not appear in the SW-scaled spectra. Spectra were obtained on a 700 MHz Bruker AV III equipped with a TCI H/C/N cryoprobe; the sample used was 40 mM gramicidin in $\text{DMSO}-d_6$.

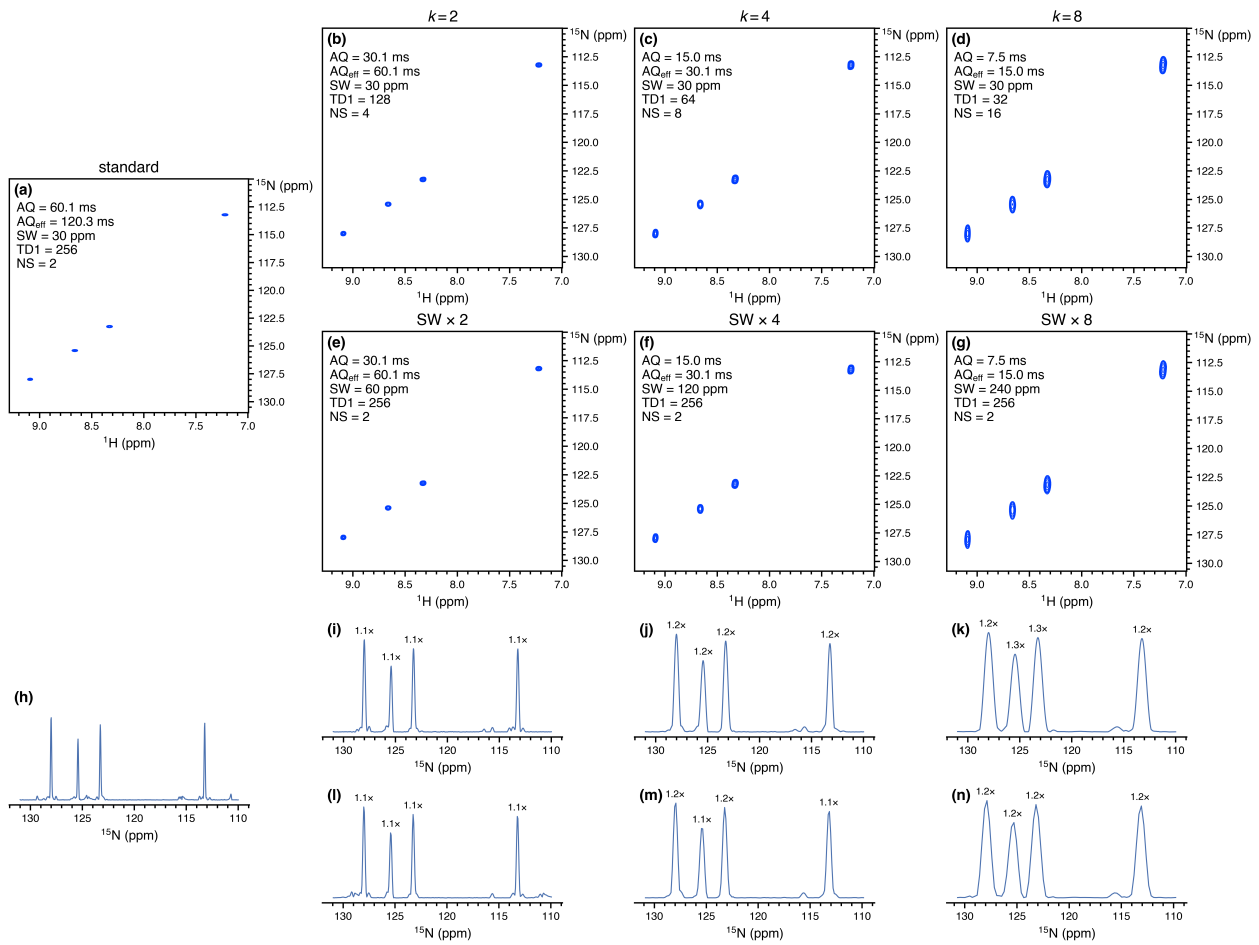


Figure S15: (seHSQC without extra linear prediction.) ^{15}N seHSQC spectra taken from NOAH-3 $\text{S}_\text{N}^+\text{S}_2^+\text{C}^\text{c}$ supersequences. All spectra are plotted with the same noise levels. No linear prediction has been applied beyond the default processing in TopSpin; thus, AQ_{eff} is $2 \times \text{AQ}$ for all of the spectra above. (a) The “standard” spectrum. (b) $k = 2$. (c) $k = 4$. (d) $k = 8$. (e) $\text{SW} \times 2$. (f) $\text{SW} \times 4$. (g) $\text{SW} \times 8$. (h)–(n) Projections of 2D spectra in (a)–(g) onto the f_1 axis. Numbers indicate peak heights relative to the “standard” seHSQC spectrum in (a). Spectra were obtained on a 700 MHz Bruker AV III equipped with a TCI H/C/N cryoprobe; the sample used was 40 mM gramicidin in $\text{DMSO}-d_6$.

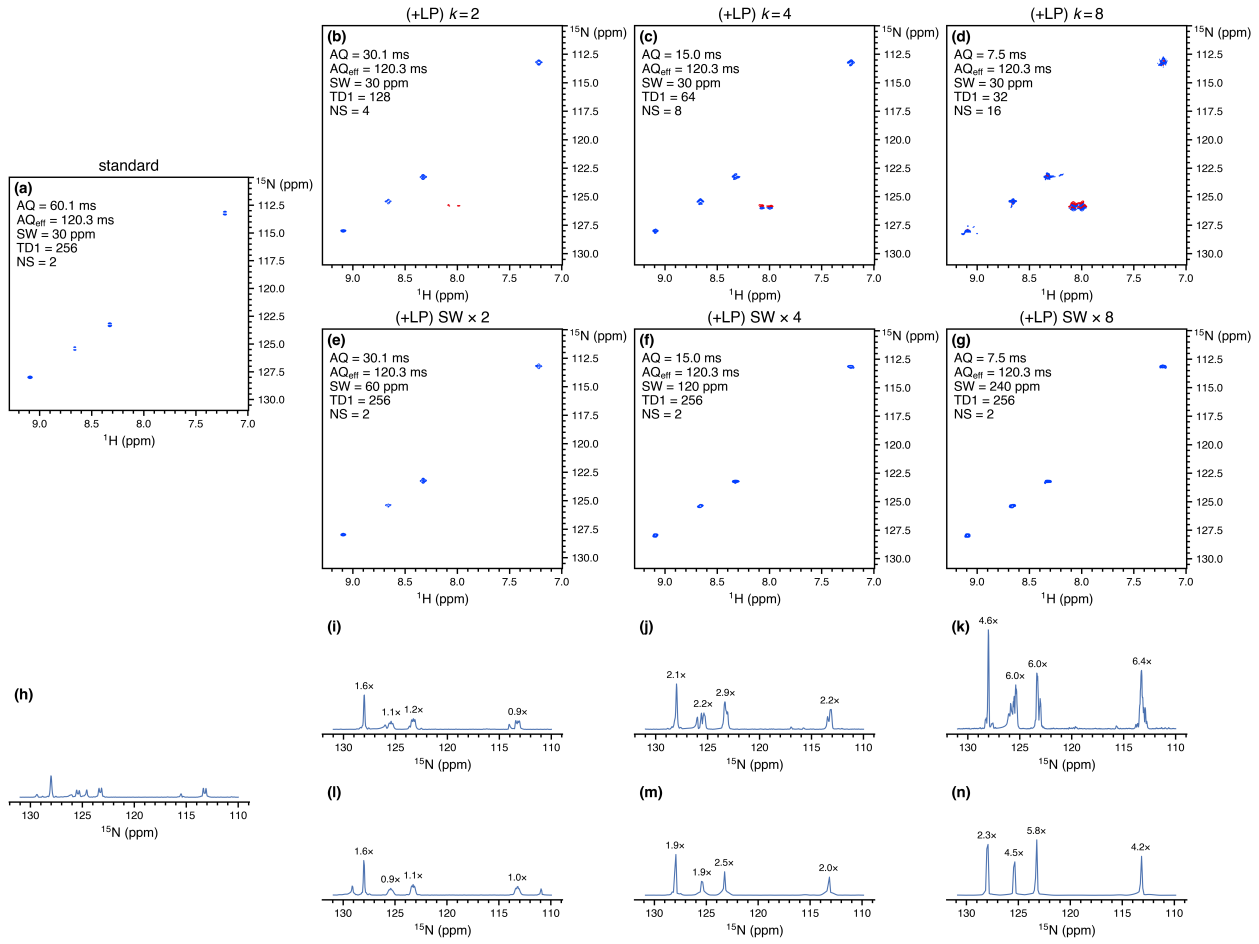


Figure S16: (HMQC with extra linear prediction.) ^{15}N HMQC spectra taken from NOAH-3 $\text{MS}_2^+\text{C}^\text{c}$ supersequences. The datasets in this figure are the same as in Figure S14: therefore, each column contains spectra which are *acquired* with the same AQ. However, in this figure, all spectra have been subjected to time-domain linear prediction up to the same AQ_{eff} of 120.3 ms. (a) The “standard” spectrum. By default, this spectrum is already linear predicted to $\text{AQ}_{\text{eff}} = 120.3$ ms; thus, this spectrum is identical to Figure S14a. (b) $k = 2$. (c) $k = 4$. (d) $k = 8$. (e) $\text{SW} \times 2$. (f) $\text{SW} \times 4$. (g) $\text{SW} \times 8$. (h)–(n) Projections of 2D spectra in (a)–(g) onto the f_1 axis. All spectra are plotted with the same noise levels. Note that linear prediction of k times more points leads to a \sqrt{k} increase in noise: so, for example, the projections in (i) and (l) (with $k = 2$ and $\text{SW} \times 2$ respectively) have $\sqrt{2}$ times more noise than the “standard” projection in (h). Numbers indicate signal-to-noise ratios relative to the “standard” HMQC spectrum in (a), obtained by dividing the relative peak height by the increase in noise. The peak at $\delta_{\text{H}} = 8.03$ ppm is folded and therefore does not appear in the SW-scaled spectra. Spectra were obtained on a 700 MHz Bruker AV III equipped with a TCI H/C/N cryoprobe; the sample used was 40 mM gramicidin in $\text{DMSO}-d_6$.

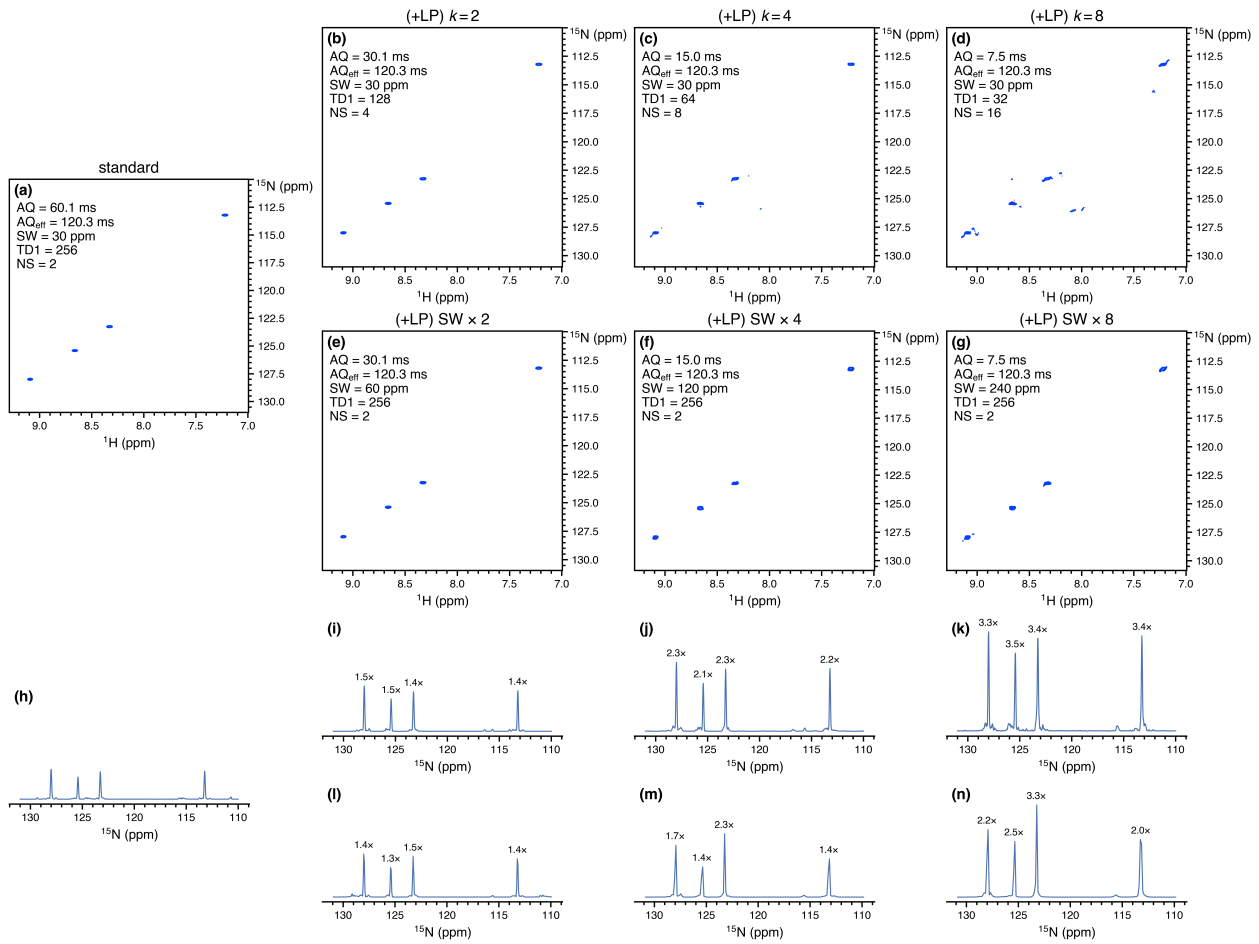


Figure S17: (seHSQC with extra linear prediction.) ^{15}N seHSQC spectra taken from NOAH-3 $\text{S}_\text{N}^+\text{S}_2^+\text{C}^\text{c}$ supersequences. The datasets in this figure are the same as in Figure S15: therefore, each column contains spectra which are *acquired* with the same AQ. However, in this figure, **all spectra have been subjected to time-domain linear prediction** up to the same AQ_{eff} of 120.3 ms. (a) The “standard” spectrum with SW = 30 ppm, $k = 1$, 256 t_1 increments (linear predicted to 512 indirect-dimension points), and 2 scans per increment (denoted as 30 : 256 : 2; AQ = 60.1 ms). (a) The “standard” spectrum. By default, this spectrum is already linear predicted to AQ_{eff} = 120.3 ms; thus, this spectrum is identical to Figure S15a. (b) $k = 2$. (c) $k = 4$. (d) $k = 8$. (e) SW $\times 2$. (f) SW $\times 4$. (g) SW $\times 8$. (h)–(n) Projections of 2D spectra in (a)–(g) onto the f_1 axis. All spectra are plotted with the same noise levels. Note that linear prediction of k times more points leads to a \sqrt{k} increase in noise: so, for example, the projections in (i) and (l) (with $k = 2$ and SW $\times 2$ respectively) have $\sqrt{2}$ times more noise than the “standard” seHSQC spectrum in (a), obtained by dividing the relative peak height by the increase in noise. The peak at $\delta_\text{H} = 8.03$ ppm is folded and therefore does not appear in the SW-scaled spectra. Spectra were obtained on a 700 MHz Bruker AV III equipped with a TCI H/C/N cryoprobe; the sample used was 40 mM gramicidin in DMSO- d_6 .

11 HSQC-TOCSY/HSQC sensitivity comparisons

The signal intensities for the NOAH-3 S^TSC^c (HSQC-TOCSY + HSQC + CLIP-COSY) supersequences can be more conveniently measured by omitting the DIPSI-2 isotropic mixing in the HSQC-TOCSY supersequence, leading to a NOAH-3 SSC^c (HSQC + HSQC + CLIP-COSY) supersequence. This allows us to compare the different versions of double-HSQC sequences, as the two HSQC modules can be implemented either using the MFA approach, or the new ASAP/NOAH approach based on Ernst angle excitation in the first module. In the latter implementation, the parameter f can be varied between 0.4 and 1; it represents the proportion of ^{13}C magnetisation used in the first HSQC, as described in the main text. Furthermore, to boost the sensitivity of the second HSQC module in the NOAH supersequences, either of the two new seHSQC modules can be used in its place: we demonstrate this here with the ZIP-seHSQC (S_2^+).

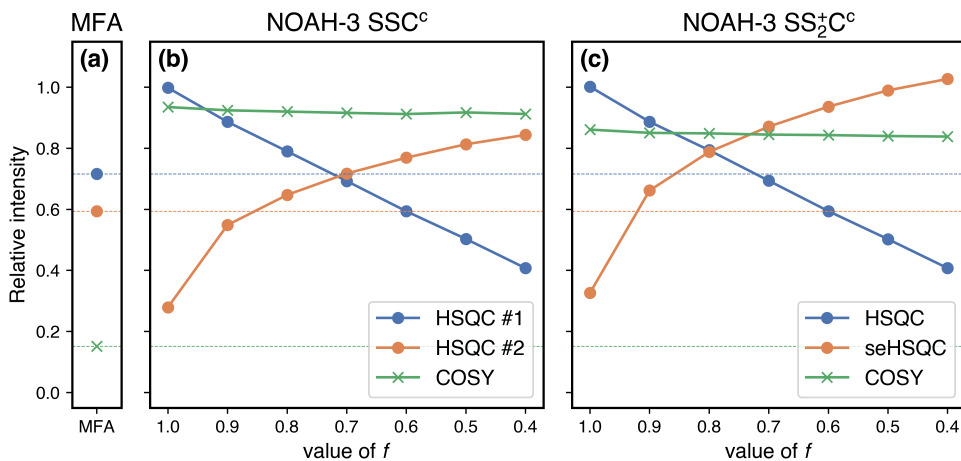


Figure S18: Sensitivities of HSQC and CLIP-COSY modules when used as part of a SSC^c-type supersequence, with both the NOAH and MFA implementations of the two HSQC modules. Intensities are calculated relative to the HSQC and CLIP-COSY modules in a standard NOAH-2 SCc supersequence (averaged over all peaks). (a) Sensitivity of the MFA implementation (i.e. a MFA double HSQC experiment immediately followed by a CLIP-COSY). Horizontal dashed lines at these levels are drawn across all subplots to guide the eye. (b) Sensitivity of NOAH-3 SSC^c modules as a function of f . Note that at $f = 0.8$, all of the NOAH spectra have a greater average sensitivity than their MFA counterparts. (c) Sensitivity of NOAH-3 SS₂^{C^c modules as a function of f . Spectra were obtained on a 700 MHz Bruker AV III equipped with a TCI H/C/N cryoprobe; the sample used was 40 mM andrographolide in DMSO-*d*₆.}

Figure S18 may be understood in the following way:

- The MFA HSQC sensitivities (in (a)) are approximately half that of a standard CRK seHSQC, with the second HSQC having slightly lower sensitivity.^[7]
- The sensitivity of the first NOAH HSQC (blue in (b) and (c)) is generally equal to f , supporting the interpretation of f as the fraction of ^{13}C - ^{1}H magnetisation excited in the first

HSQC.

- The sensitivity of the second NOAH HSQC (orange in (b)) arises from whatever is *not* used by the first HSQC, plus any magnetisation that recovers during the FID of the first HSQC. As f is decreased, the former contribution increases and the latter tapers off. This is true for the seHSQC as well (orange in (c)), except that there is a uniform boost in sensitivity for all values of f . This sensitivity improvement mainly applies to CH groups, as discussed in the main text.
- The MFA COSY sensitivity (green) is substantially lower ($\sim 15\%$) because the bulk magnetisation is dephased by the previous modules, whereas in the NOAH approach it is (largely) preserved.

It remains to evaluate the impact of adding DIPSI-2 mixing in one of the HSQC modules on the remaining modules in the supersequence. This depends on whether the HSQC-TOCSY module is placed first (S^TSC^c or $S^TS_2^+C^c$) or second (SS^TC^c) in the sequence. Since neither of the new seHSQC modules do preserve unused $^1H^C$ magnetisation, the HSQC-TOCSY in a hypothetical $S^+S^TC^c$ supersequence will have greatly reduced sensitivity. On the other hand, placing the HSQC-TOCSY sequence first allows the seHSQC module to be used subsequent to this; we therefore consider only the permutations where the HSQC-TOCSY goes first.

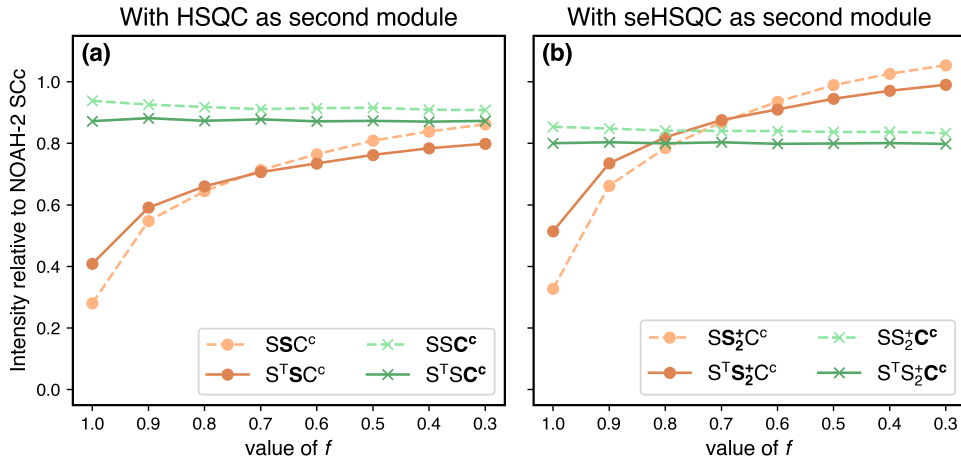


Figure S19: Comparison of signal intensities of second (HSQC or seHSQC) and third (CLIP-COSY) modules in the $STSC^c$ and $STS_2^+C^c$ supersequences, versus their intensities in the SSC^c and $SS_2^+C^c$ sequences, as a function of the parameter f . The solid, darker lines indicate the supersequences beginning with the HSQC-TOCSY, whereas the dashed, lighter lines indicate the supersequences beginning with the HSQC (the latter are the same graphs as in Figure S18). (a) With the HSQC as the second module. (b) With the seHSQC as the second module. Spectra were obtained on a 700 MHz Bruker AV III equipped with a TCI H/C/N cryoprobe; the sample used was 40 mM andrographolide in $DMSO-d_6$.

It can be seen from Figure S19 that the introduction of DIPSI-2 mixing leads to a very small drop

($< 10\%$) in the amount of $^1\text{H}^{1\text{C}}$ magnetisation preserved for the COSY module. On the other hand, the HSQC (and seHSQC) sensitivities follow largely the same trend as before. For values of f above 0.7 (where relatively little $^1\text{H}^{1\text{C}}$ magnetisation is preserved for these modules), the DIPSI-2 mixing helps to replenish some of this magnetisation. As f decreases, this effect becomes smaller, and at $f < 0.7$ it even leads to a *reduction* in signal intensity (i.e. where the orange lines cross in Figure S19).

As discussed in the main text, since the HSQC-TOCSY has a lower intrinsic sensitivity than the (se)HSQC, we recommend using a large value of f , such as 0.9. This does not compromise the HSQC-TOCSY intensity by much, and at the same time yields either a HSQC with $\sim 60\%$ of its original sensitivity, or a seHSQC which has $\sim 75\%$ of the sensitivity of a standalone NOAH HSQC module. However, if the sensitivity of the HSQC-TOCSY component is to be maximised, then it is advisable to use the seHSQC-TOCSY module, which is based on the S_2^+ module.^[8] This module cannot preserve any $^1\text{H}^{1\text{C}}$ magnetisation for the downstream HSQC, but does retain $^1\text{H}^{1\text{C}}$ magnetisation for homonuclear modules: its performance in this respect is therefore very similar to the HSQC-TOCSY with $f = 1$ (Figure S20). However, it provides greater sensitivity in the HSQC-TOCSY component itself, so is strictly better than the HSQC-TOCSY with $f = 1$.

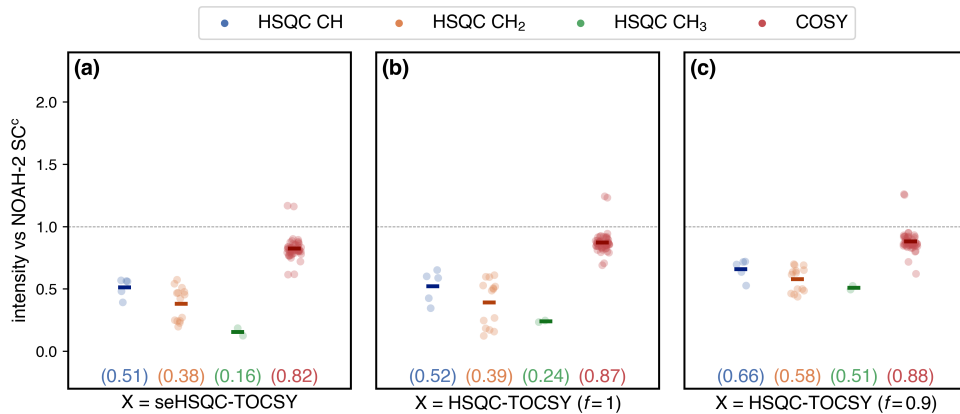


Figure S20: HSQC and COSY intensities in NOAH-3 XSC^c supersequences, where X is a HSQC-TOCSY variant, normalised against the intensities of the NOAH-2 SC^c. (a) With X as the seHSQC-TOCSY module, derived from the S_2^+ sequence. (b) With the unenhanced HSQC-TOCSY module ($f = 1$). Note that this provides no improvement over the seHSQC-TOCSY in the downstream HSQC and COSY modules. (c) With the unenhanced HSQC-TOCSY module ($f = 0.9$). This retains a portion of unused $^1\text{H}^{1\text{C}}$ magnetisation for the second HSQC, resulting in higher intensities. Spectra were obtained on a 700 MHz Bruker AV III equipped with a TCI H/C/N cryoprobe; the sample used was 40 mM andrographolide in DMSO-*d*₆.

Finally, we note that because a significant proportion of the HSQC signal derives from $^1\text{H}^{1\text{C}}$ relaxation during the HSQC-TOCSY FID, use of a longer AQ can potentially boost the HSQC sensitivity even further. The experiments shown above were carried out with a relatively short AQ of 73 ms. **However, bear in mind that the high duty cycle associated with broadband ^{13}C decou-**

pling can potentially damage the probe if applied for too long, especially given that the supersequences described here have two consecutive ^{13}C -decoupled modules.

12 Other example spectra

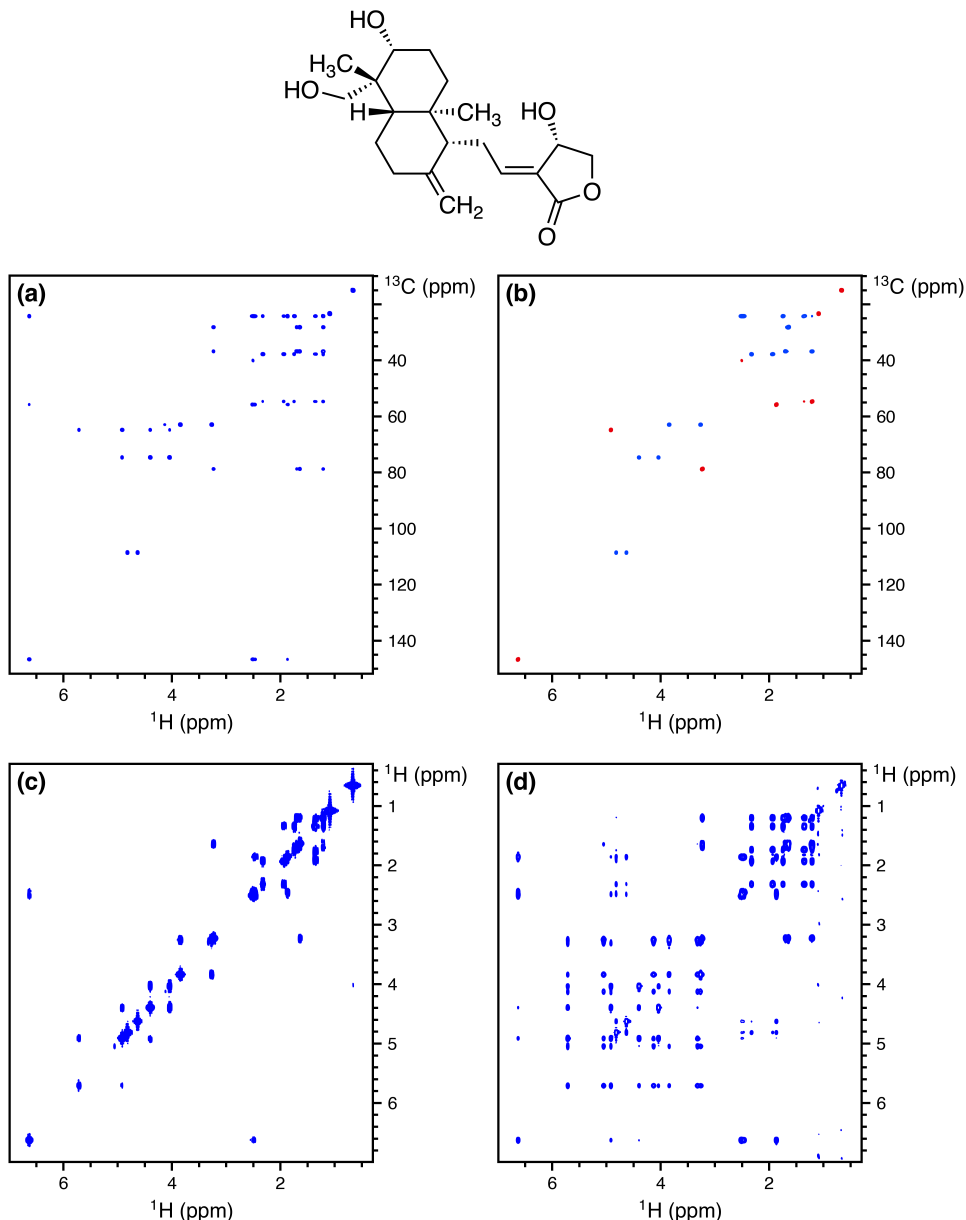


Figure S21: 2D spectra acquired using the NOAH-4 $\text{S}^T\text{S}_2^+\text{CT}$ supersequence. 256 t_1 increments were used with 2 scans per increment, leading to a total experiment time of 17 minutes and 32 seconds. This represents a 3.25 \times time saving relative to conventional acquisition of each of the four spectra with the same parameters, which would take a total of 57 minutes and 3 seconds. (a) HSQC-TOCSY (30 ms mixing time, $f = 0.9$). (b) Multiplicity edited seHSQC. (c) COSY. (d) TOCSY (60 ms mixing time). Spectra were obtained on a 700 MHz Bruker AV III equipped with a TCI H/C/N cryoprobe; the sample used was 40 mM andrographolide in $\text{DMSO}-d_6$.

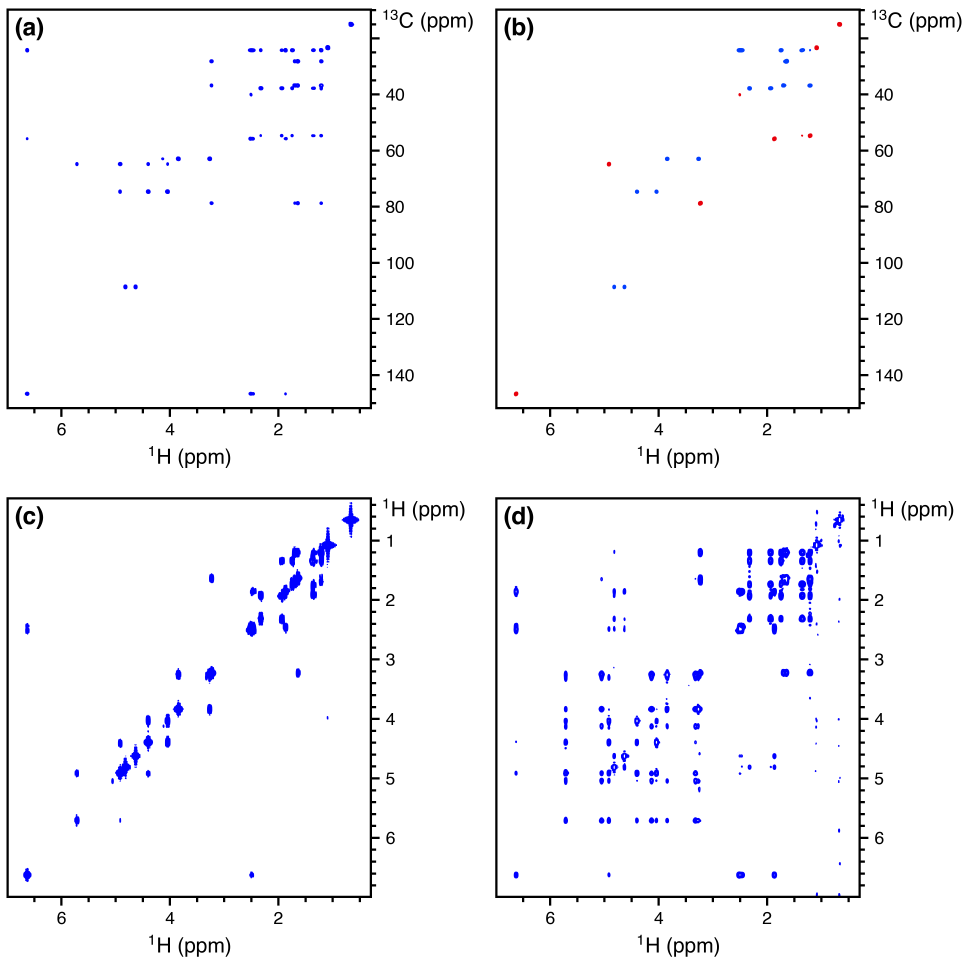
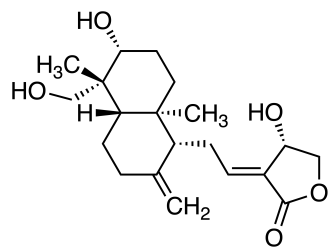


Figure S22: 2D spectra acquired using the NOAH-4 S^TS₂⁺CT supersequence with 50% non-uniform sampling for all modules. All other parameters are the same as in Figure S21. The experimental time was 9 minutes and 1 second. (a) HSQC-TOCSY (30 ms mixing time, $f = 0.9$). (b) Multiplicity edited seHSQC. (c) COSY. (d) TOCSY (60 ms mixing time). Spectra were obtained on a 700 MHz Bruker AV III equipped with a TCI H/C/N cryoprobe; the sample used was 40 mM andrographolide in DMSO-*d*₆.

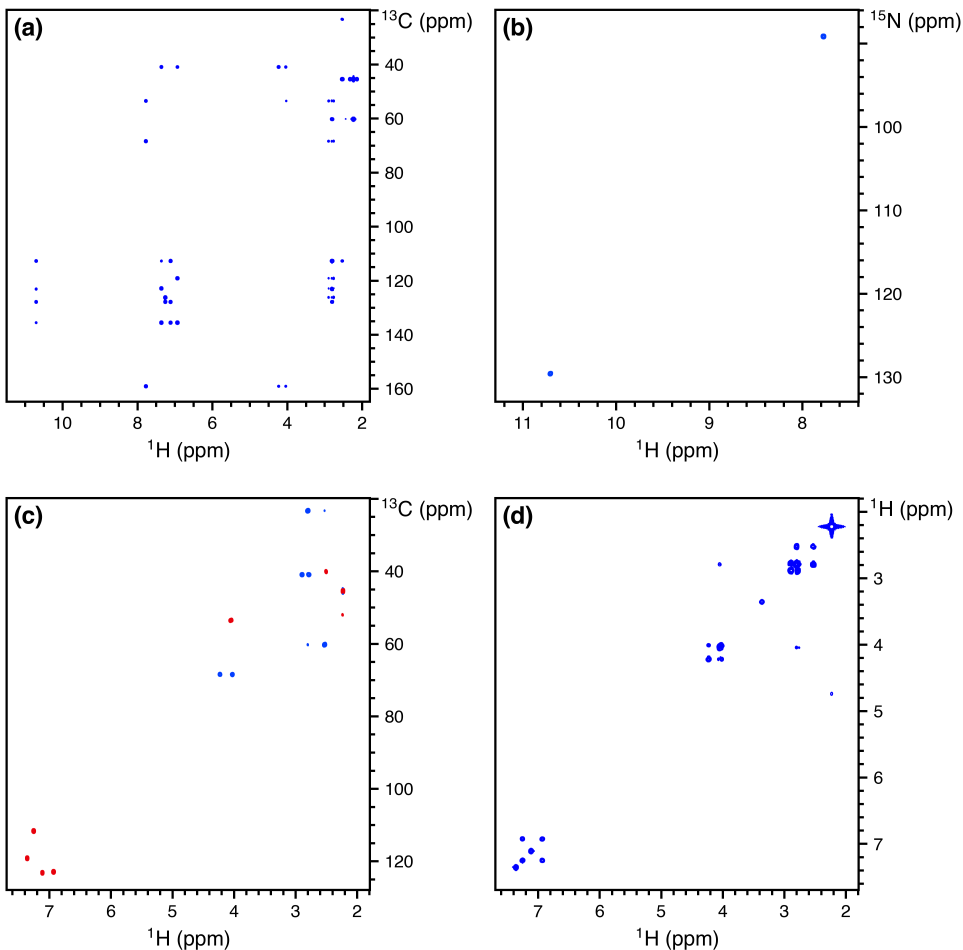
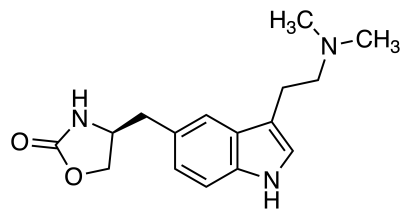


Figure S23: 2D spectra acquired using the NOAH-4 $\text{BS}_{\text{N}_2}^+ \text{S}_2^+ \text{C}$ supersequence. 256 t_1 increments were used with 2 scans per increment, leading to a total experiment time of 17 minutes and 32 seconds. This represents a 3.22 \times time saving relative to conventional acquisition of each of the four spectra with the same parameters, which would take a total of 56 minutes and 28 seconds. (a) HMBC. (b) ^{15}N seHSQC with $k = 4$, linear predicted to 512 complex points. (c) Multiplicity edited ^{13}C seHSQC. (d) Magnitude-mode COSY (Bruker qf mode). Spectra were obtained on a 700 MHz Bruker AV III equipped with a TCI H/C/N cryoprobe; the sample used was 50 mM zolmitriptan in $\text{DMSO}-d_6$.

13 Sensitivity per unit time gains

Whilst we have so far mainly focused on the *time savings* that can be achieved via NOAH supersequences, it should also be noted that time savings can be translated into gains in sensitivity per unit time, according to the formula:^[9]

$$\varepsilon_t = R_S \cdot \sqrt{\rho_t}$$

where ε_t is the relative sensitivity per unit time, ρ_t is the time saving factor (i.e. the total experimental time needed for conventional acquisition, divided by the duration of the NOAH supersequence), and R_S is a factor indicating the relative sensitivity of the NOAH module compared to a reference experiment. R_S may in general be less than 1 due to several factors:

1. Imperfect retention of magnetisation by previous modules in a supersequence will reduce the value of R_S for downstream modules. The resulting value of R_S may range from ~ 0.9 (HSQC without sensitivity enhancement) to ~ 0.1 (CRK seHSQC), as shown in Table S2.
2. Any modifications made to the sequence in order to achieve other aims such as artefact suppression or preservation of unused magnetisation components may lead to loss of signal. This is the case with, for example, the NOAH seHSQC modules, which have lower sensitivity compared to the original CRK implementation (Figures 2 and S12).

The value of R_S for a given module therefore depends on each of the previous modules in a supersequence. Since R_S differs for each module in a supersequence, so does ε_t ; if $\varepsilon_t > 1$ for a given module, then the supersequence can provide an increase in sensitivity per unit time for that module.

In Figure 6 we demonstrated that $\varepsilon_t > 1$ for all four modules in the $S_N^+S_2^+$ CT supersequence. The reference spectra there were taken to be the standalone NOAH modules, acquired as a set of four individual 2D experiments: thus, any reductions from R_S must arise solely from item (1) above, as the sequences themselves are identical.

In Figure S24, we perform the same comparison but this time using the “gold standard” 2D experiments (such as the CRK seHSQC) as the reference experiments: details of these experiments are provided in Table S3. This, together with the other SNR comparisons provided in this work, provide a measure of the losses in R_S due to item (2) above. Thus, the values of ε_t are lower than in Figure 6. However, we notably still have $\varepsilon_t > 1$ for the first three modules, and $\varepsilon_t \sim 1$ for the TOCSY, proving that NOAH supersequences do provide gains in sensitivity per unit time compared to conventional acquisition.

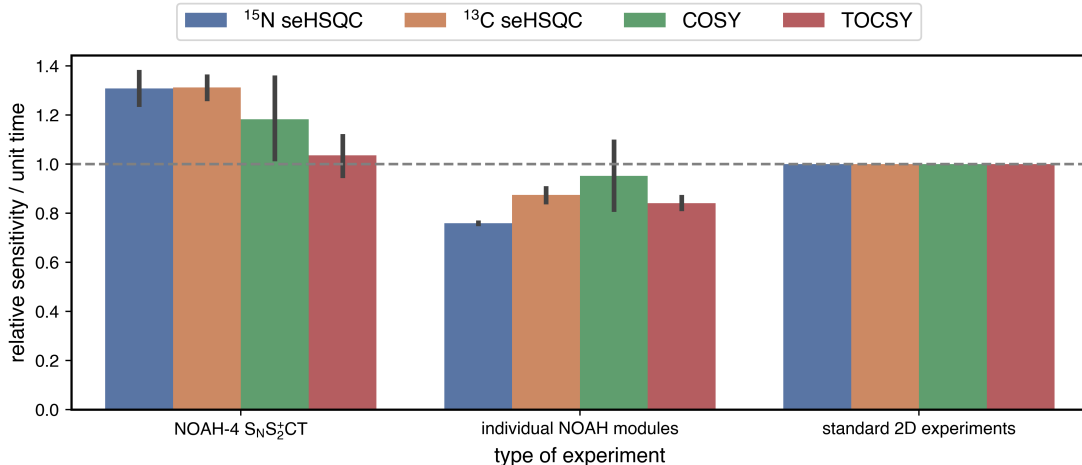


Figure S24: Relative sensitivities per unit time (ε_t) for the four modules in the $\text{S}_\text{N}^+ \text{S}_2^+ \text{CT}$ supersequence (using a TOCSY mixing time of 35 ms). Error bars indicate 95% confidence intervals. Individually acquired standard 2D spectra were used as the reference spectra ($\rho_t = 3.24$). Spectra were obtained on a 700 MHz Bruker AV III equipped with a TCI H/C/N cryoprobe; the sample used was 50 mM zolmitriptan in $\text{DMSO}-d_6$.

Experiment	Duration				Total
	^{15}N seHSQC	^{13}C seHSQC	COSY	TOCSY	
NOAH-4					
					17 min 28 s
Individual modules	14 min 36 s	14 min 26 s	14 min 13 s	15 min 27 s	58 min 42 s
Standard 2Ds					
hsqcetf3gpsi2	14 min 5 s				
hsqcedetgpsisp2.3		14 min 1 s			
cosygpqf			13 min 57 s		
dipsi2gpphzs				14 min 32 s	

Table S3: Details of experiment times and pulse sequences used for comparisons of sensitivity per unit time (Figures 6 and S24). Spectra were obtained on a 700 MHz Bruker AV III equipped with a TCI H/C/N cryoprobe; the sample used was 50 mM zolmitriptan in $\text{DMSO}-d_6$.

References

- [1] (a) Ě. Kupče, R. Freeman, *J. Am. Chem. Soc.* **2004**, *126*, 6429–6440; (b) S. Hiller, F. Fiorito, K. Wuthrich, G. Wider, *Proc. Natl. Acad. Sci. U. S. A.* **2005**, *102*, 10876–10881.
- [2] J. Schleucher, M. Schwendinger, M. Sattler, P. Schmidt, O. Schedletzky, S. J. Glaser, O. W. Sørensen, C. Griesinger, *J. Biomol. NMR* **1994**, *4*, 301–306.
- [3] M. Pérez-Trujillo, P. Nolis, W. Bermel, T. Parella, *Magn. Reson. Chem.* **2007**, *45*, 325–329.
- [4] T. Parella, P. Nolis, *Concepts Magn. Reson.* **2010**, *36A*, 1–23.
- [5] (a) D. L. Donoho, I. M. Johnstone, A. S. Stern, J. C. Hoch, *Proc. Natl. Acad. Sci. U. S. A.* **1990**, *87*, 5066–5068; (b) A. S. Stern, K.-B. Li, J. C. Hoch, *J. Am. Chem. Soc.* **2002**, *124*, 1982–1993; (c) M. R. Palmer, C. L. Suiter, G. E. Henry, J. Rovnyak, J. C. Hoch, T. Polenova, D. Rovnyak, *J. Phys. Chem. B* **2015**, *119*, 6502–6515.
- [6] M. Mobli, J. C. Hoch, *Prog. Nucl. Magn. Reson. Spectrosc.* **2014**, *83*, 21–41.
- [7] P. Nolis, K. Motiram-Corral, M. Pérez-Trujillo, T. Parella, *ChemPhysChem* **2019**, *20*, 356–360.
- [8] A. L. Hansen, Ě. Kupče, D.-W. Li, L. Bruschweiler-Li, C. Wang, R. Brüschweiler, “2D NMR-based Metabolomics with HSQC/TOCSY NOAH Supersequences”, submitted for publication, **2021**.
- [9] Ě. Kupče, T. D. W. Claridge, *J. Magn. Reson.* **2019**, *307*, 106568.